Continental Shelf Research 215 (2021) 104348

Contents lists available at ScienceDirect

Continental Shelf Research

journal homepage: http://www.elsevier.com/locate/csr

CO_2 partial pressure and fluxes in the Amazon River plume using in situ and remote sensing data

Aline M. Valerio [a,*], Milton Kampel [a], Nicholas D. Ward [b,c], Henrique O. Sawakuchi [d], Alan C. Cunha [e], Jeffrey E. Richey [c]

[a] National Institute for Space Research, Avenida Dos Astronautas, 1758, São José Dos Campos, SP, Brazil
[b] Marine Science Laboratory, Pacific Northwest National Laboratory, 1529 W Sequim Bay Rd, Sequim, WA, USA
[c] School of Oceanography, University of Washington, 1501 NE Boat St, Seattle, WA, USA
[d] Department of Thematic Studies – Environmental Change, Linköping University, Linköping, SE-581 83, Sweden
[e] Department of Exact and Technological Sciences, Federal University of Amapá, Rod. Juscelino Kubitschek, Km 02, Macapá, AP, Brazil

ARTICLE INFO

Keywords:
Amazon river plume
pCO_2
Carbon dioxide
Sea surface temperature
Sea surface salinity
SMOS

ABSTRACT

Estimations of the global carbon budget include a quantitative understanding of the evolving processes that occur along river-to-ocean gradients. However, high spatiotemporal resolution observations of these processes are limited. Here we present in situ measurements of the partial pressure of CO_2 (pCO_2) made through the Amazon River plume (ARP) during different discharge seasons, from 2010 to 2012. We evaluated the spatiotemporal distribution of pCO_2 using Soil Moisture and Ocean Salinity (SMOS) satellite observations for each hydrologic period in the ARP. Regression models were used to estimate pCO_2 at the ARP for the period of 2010–2014. From these distributions we calculated sea-air gas exchange of CO_2 between the plume waters and the atmosphere (F^{sea}_{co2}). Intra-annual variability of F^{sea}_{co2} was related to discharge at the river mouth and ocean currents as well as trade winds in the plume. Climatic events during the study period had a significant impact on the F^{sea}_{co2}. Including the plume area closer to the river mouth makes the ARP a net source of CO_2 with an annual net sea-air flux of 8.6 ± 7.1 Tg C y^{-1} from 2011 to 2014.

1. Introduction

Inland waters and coastal oceans are becoming increasingly recognized as integrated water systems through which geochemical constituents are constantly transformed providing unique biogeochemical influences in different sectors along the continuum (Hedges et al., 1997; Dagg et al., 2004; Medeiros et al., 2015; Arellano et al., 2019; Ward et al., 2017). However, few studies have addressed the spatial and temporal dynamics of water and carbon fluxes from the mouth of major river systems out into marine receiving waters. Rivers usually act as a pump of CO_2 that transfers carbon dioxide from the water to the atmosphere (Cole et al., 2007; Tranvik et al., 2009; Raymond et al., 2013) largely due to the breakdown of terrestrially-derived organic matter (Ward et al., 2013) and floodplain inputs (Abril et al., 2014). Conversely, river-dominated coastal areas such as the Amazon River plume (ARP) are typically thought to remove CO_2 from the atmosphere due to enhanced primary production driven by fluvial nutrients (Cooley et al., 2007; Subramaniam et al., 2008; Yeung et al., 2012; Goes et al., 2014; Gouveia et al., 2019).

Draining an area of ~6.5 million km^2, the Amazon basin represents ~20% of all freshwater discharge to the global ocean and ~44% of global evasive CO_2 gas flux from inland waters (Richey et al. 1990, 2002; Raymond et al., 2013; Sawakuchi et al., 2017). The Amazon River plume extends up to 10^6 km^2 over the Western Tropical Atlantic (WTNA) (Molleri et al., 2010), reaching the Caribbean Sea (Müller-Karger et al., 1989). The ARP flows into the WTNA near the equator and is transported northwestwards by the North Brazil Current (NBC) along the Brazilian north shelf (Müller-Karger et al., 1988; Molleri et al., 2010; Salisburry et al., 2011).

Based on measurements of the outer plume, a net carbon sequestration as high as ~27 Tg C yr^{-1} from the atmosphere was estimated and mainly accounted for primary production in the mesohaline area (salinity = 30–35) (Cooley et al., 2007; Subramaniam et al., 2008). Lefèvre et al. (2010) estimated an annual CO_2 flux of 5 Tg C yr^{-1} from the atmosphere into the ARP. Conversely, the Amazon River basin (streams, rivers, floodplains, lakes) outgasses on the order of ~500 Tg C

* Corresponding author.
E-mail address: aline.valerio@inpe.br (A.M. Valerio).

https://doi.org/10.1016/j.csr.2021.104348
Received 8 May 2020; Received in revised form 11 December 2020; Accepted 7 January 2021
Available online 13 January 2021

yr^{-1} CO_2 (Richey et al., 2002) to ~1800 Tg C yr^{-1} (Melack 2016; Sawakuchi et al., 2017). This poses the question, what happens to CO_2 fluxes across the continuum, from river export to the overall ARP, on a seasonal basis?

This study evaluates the potential overall net flux of CO_2 across the Amazon River plume, from the outer plume to within 100 km of the coastline. Even with some geographical limitation of the satellite data used, part of the innermost plume is considered in the present study, complementing previous studies in this area. We hypothesize that the CO_2 input from the Amazon River is high enough to offset CO_2 absorption in the outer plume.

Answering the question about what happens to CO_2 fluxes across the continuum poses a significant logistical challenge of enough spatial-temporal coverage to adequately characterize overall flux patterns. Quantitative linkages between remotely sensed products and in situ pCO_2 measurements provide a synoptic view of main processes over a large spatial area, and a more holistic view of the variability and dynamics of net sea-air CO_2 fluxes compared to what can be inferred from in situ ship measurements alone. The integrated approach can provide more accurate estimations of large-scale regional fluxes. Further, if an established relationship between pCO_2 and remotely-sensed parameters is robust and representative of an area beyond a particular sampling period, longer term variability can be assessed both in present and in past times. Thus, the influence of environmental factors such as flood/drought cycles and climatic events such as El Niño Southern Oscillation (ENSO) on CO_2 fluxes can be studied.

Several studies have attempted to estimate pCO_2 from remotely sensed products and later compute the sea-air CO_2 flux. Sea Surface Temperature (SST) (Lohrenz and Cai 2006; Zhu et al., 2009; Bai et al., 2015; Liu and Xie 2017) and Chlorophyll-*a* concentration (Chl-*a*) (Hales et al., 2012; Signorini et al., 2013) are the remotely-sensed products mostly used to relate with in situ pCO_2 by linear or multiple regression. To improve the relationship, other remote sensing products have been also considered such as Sea Surface Salinity (SSS) (Bai et al., 2015; Ibánhez et al., 2015; Liu and Xie 2017; Joshi et al., 2018) and light absorption by colored dissolved organic matter (CDOM) (Lohrenz and Cai 2006). To compute sea-air CO_2 fluxes from pCO_2 estimates, ocean surface wind vectors have been used (Zhu et al., 2009; Ibánhez et al., 2015; Lohrenz et al., 2018). Other statistical methods besides linear or multiple regression have also been applied, such as principal component analysis (Lohrenz and Cai 2006), neural networks (Telszewski et al., 2009; Hales et al., 2012; Landschützer et al., 2014) and semi-analytical algorithms (Bai et al., 2015; Song et al., 2016). The present analysis is based on the correlation between remotely-sensed SSS and SST from the Soil Moisture and Ocean Salinity (SMOS) satellite and in situ pCO_2 measurements.

2. Materials and Methods

2.1. Sampling and study area

The NBC is a low latitude strong western-boundary current (Fratantoni and Richardson, 2006; Akuetevi and Wirth, 2015) that retroflects in July–September near 6–8°N and separates away from the boundary, turning anti-cyclonically for more than 90°. It forms anticyclonic eddies exceeding 450 km in diameter (Richardson et al., 1994; Garzoli et al., 2004). The NBC retroflection with a fraction of the ARP feeds the North Equatorial Counter Current (Johns et al., 1998), an eastward zonal current that contributes to the formation of the anticyclonic current rings (Castelão and Johns, 2011). In December–March, the ARP is trapped in the river mouth due to onshore blowing trade winds (Lentz and Limeburner 1995).

The dispersal of the ARP is directly impacted by trade wind variability and seasonal migration of the Intertropical Convergence Zone (ITCZ) from its northern position in boreal summer to its southern position in boreal winter (Xie and Carton, 2004), changing the net heat flux and wind fields in the WTNA (Coles et al., 2013; Fournier et al., 2017). This seasonal behaviour of the ARP has ecological implications for the WTNA, reflecting the response of the phytoplankton community to changing nutrients availability (Smith and DeMaster, 1996), freshwater river outflow into the ocean (Coles et al., 2013), and consequently, affecting carbon dioxide fluxes (Cooley et al., 2007).

Three oceanographic cruises (R/V Knorr KN197 – June of 2010; R/V Melville MV1110 - September to October 2011; R/V Atlantis AT21–04 July of 2012) were performed in the study area (Fig. 1(a)) during high, low, and falling river discharge periods (Table 1; Fig. 1(b)). The geographical limits of the study area were defined as 15°N-5°S; 60°W-45°W for comparison with previous studies in the same area (Cooley et al., 2007; Subramaniam et al., 2008; Yeung et al., 2012; Goes et al., 2014).

This study considers the river plume as the area covered by surface water with SSS <35 for consistency with prior studies that established this threshold for the ARP (Coles et al., 2013; Grodsky et al., 2014; Ibánhez et al. 2015, 2016). In addition to the years of in situ sampling, our analysis also covers the years of 2013 and 2014, as the remote sensing products used were available for the years of 2010–2014 (see more in section 2.3).

The year 2010 was characterized by a severe drought in the Amazon region due to a strong El Niño event (Marengo et al., 2011). However, the 2012–2014 period included a record flood in the Amazon Basin that started with a La Niña event in 2012 and continued with a positive SST anomaly in the tropical Atlantic, south of the equator and in the Western Tropical Pacific (Satyamurty et al., 2013; Espinoza et al., 2014; Marengo and Espinoza 2016).

2.2. Field measurements

Salinity and water temperature underway data were collected during the three cruises. Surface pCO_2 observations were collected using an underway pCO_2 system with a non-dispersive infrared CO_2 gas analyzer (LI-COR 6252) and standardized using CO_2-air reference gas mixtures from National Oceanic and Atmospheric Administration (NOAA) Climate Monitoring and Diagnostics Laboratory (CMDL). The in situ oceanographic data consists of 15,392 data points, taken every 10 min during the three cruises. In situ pCO_2 measurements from the transects are shown in the supplement material (Figure A1).

2.3. Remote sensing products

The Soil Moisture and Ocean Salinity (SMOS) mission measures microwave radiation emitted from the Earth' surface around 1.4 GHz (L-band), using the 2D Microwave Imaging Radiometer with Aperture Synthesis (MIRAS). SMOS was launched on November 2009 and initially provided data to the scientific community in May 2010 (Mecklenburg et al., 2012; Reul et al., 2012). The daily Level 3 product with 0.5 degree of spatial resolution delivered by the Centre National d' Etudes Spatiales - Institut Français de Recherche pour l' Exploitation de la Mer (CNES-IFREMER) was available for 2010–2014. The selected product provides SSS, SST and Wind Speed (WS) data. SSS is a parameter provided by SMOS, while SST and WS were obtained from the European Centre for Medium-Range Weather Forecast (ECMWF) analysis. SST is based on the Operational Sea Surface Temperature and Sea Ice Analysis (OSTIA) system (Donlon et al., 2012). WS is provided by the ECMWF Meteorological Archival and Retrieval System (Yin et al., 2014).

SMOS products were acquired concomitantly ±1 day around in situ sampling dates, to avoid missing data due to the 3 days revisit time of SMOS. The products were further processed using the Sea-viewing Wide Field-of view Sensor (SeaWiFS) Data Analysis System (SeaDAS) v.7.3.1 software provided by NASA. All images were cropped for the WTNA area, and the math band function was used to calculate the pCO_2 and the sea-air CO_2 flux for the Amazon River plume. To aggregate multiple files with corresponding bands into a single mapped file, the mosaic function

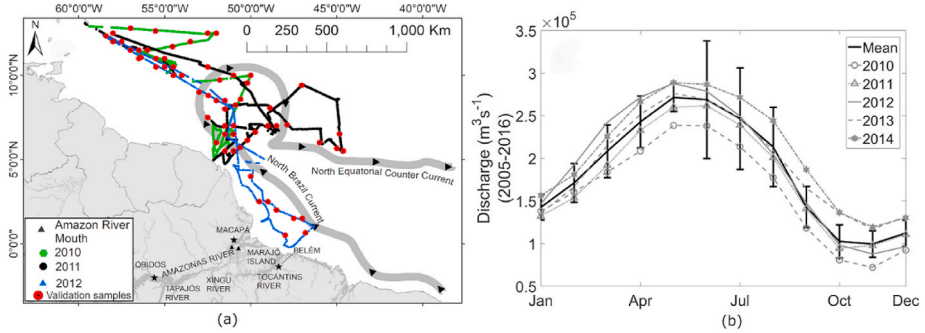

Fig. 1. Study area. (a) Overall study area showing the in situ sampling oceanographic routes during 2010–2012. (b) Amazon River discharge in the study period (2010–2014) showing the mean and standard deviation monthly historical discharge (2005–2016) at Óbidos (data from the Agência Nacional de Águas, http://hidroweb.ana.gov.br).

Table 1
Dates of in situ data sampling conducted in the study area with its respective discharge season.

Dates	Discharge Season
05–23 June 2010	High
02 Sep - 06 Oct 2011	Low
13–29 Jul 2012	Falling

was used for the three-month composite images according to the Amazon River discharge season. SMOS has a drawback due to a higher microwave brightness temperature of the land, which contaminates the ocean signal leading to inaccurate near-shore SSS values (Talone et al., 2009). Thus, we restricted its use to beyond 100 km offshore. A consequence is that the plume within 100 km of the coast is not included in the analysis.

SMOS data has been previously used to obtain sea-air CO_2 fluxes (Ibánhez et al., 2016) and parameters of the marine carbonate system such as total alkalinity and dissolved organic carbon with satisfactory performance (Land et al., 2019). The use of SMOS data instead of a ocean colour sensor was necessary because of the lack of availability of bio-optical data sufficiently representative of the study region, or in particular, the inner Amazon River plume area to develop and validate a pCO_2 predictive algorithm. To our knowledge, available databases such as NASA's SeaBASS (seabass.gsfc.nasa.gov) do not cover the plume area closer to the Amazon River mouth addressed in this study.

2.4. pCO_2 predictive algorithm

A predictive algorithm was developed based on the relationship between in situ SSS, SST and pCO_2 data using a multiple polynomial regression model. SSS and SST have been shown to correlate with the variability of pCO_2 (Lohrenz and Cai 2006; Zhu et al., 2009; Ibánhez et al., 2015; Bai et al., 2015), although the relationship between SSS and pCO_2 is much more evident in the ARP (Ternon et al., 2000). While many different approaches have been used to estimate and map coastal pCO_2, they are all relatively consistent with previous estimations for the same area and season (Rödenbeck et al., 2015). These estimations of pCO_2 are often performed for oceanic waters and when developed for river plumes, samples are usually collected at the distal plume area. In this border area, nutrient and sediment rich river water is more dilute and provides a better environment for phytoplankton blooms, and consequently, CO_2 consumption, resulting in the transfer of atmospheric CO_2 into the water. This is a bias to be considered when developing a predictive algorithm of pCO_2, and for that reason, we developed a new algorithm that considers an inner area of the ARP closer to the river mouth.

Underway salinity, water temperature and pCO_2 measurements along the tracks of the three cruises were averaged for every pixel of the SMOS daily products (N = 318) for the respective cruise date (±1day), and from here these variables will be here denominated as SSS_i, SST_i and pCO_{2i}. The variability of these in situ data within the SMOS pixel was calculated as the coefficient of variation (Equation (1)):

$$cv = \frac{\sigma}{\mu} \quad (1)$$

where σ is the standard deviation and μ is the average of all in situ data within the SMOS pixel.

A limitation faced using our dataset is the poor performance of SMOS to retrieve lower values of salinity (<30) (Fig. 4(a)). The error of SSS increased closer to the river mouth (as propagated in our calculations). Therefore, in situ salinity samples considered outliers were discarded after a Cook's distance analysis, which has a cutoff of three times the mean Cook's distance. Samples from 2012 obtained at less than 100 km from the coastline were excluded before averaging in situ data and removal of outliers, because they were outside the limits of SMOS products. The outlier removal produced 253 final samples (pixels with corresponding averaged in situ data), where 70% of the samples were partitioned to generate the model using the multiple polynomial regression model, and 30% were used for validation (N_{model} = 177; $N_{validation}$ = 76).

The resultant formula was applied to SMOS daily data of the same dates of in situ sampling to generate pCO_2 remote sensing products and to validate the model. The predictive algorithm was applied to three-month composites of SMOS data for 2010–2014.

2.5. Sea-air CO_2 flux

The CO_2 flux from the sea-air CO_2 exchange, F_{co2}^{sea} (mmol m^{-2} d^{-1}) in the ARP was calculated according to Wanninkhof (1992) (Equation (2)):

$$F_{co2}^{sea} = k_{co2} K_0 \left(pCO_2^{sea} - pCO_2^{air}\right) \quad (2)$$

where pCO_2 is the partial pressure of CO_2 (μatm), k_{co2} (cm hr^{-1}) is the gas transfer coefficient and K_0 (mol $L^{-1}atm^{-1}$) is the solubility of CO_2. Negative values of F_{co2}^{sea} indicate that the water acts as a carbon sink while positive values indicate that water acts as a source of carbon to the atmosphere. pCO_2^{air} was calculated using the monthly atmospheric molar fraction of CO_2 (xCO_2) (Equation (3)) obtained from Barbados (13.17°N-59.43°W), the closest station of the NOAA Earth System Research Laboratory (ESRL) Global Monitoring Division:

$$pCO_2 = xCO_2 (P_{atm} - P_{water}) \quad (3)$$

where P_{atm} is the barometric pressure and P_{water} is the water vapor pressure calculated from the measured SST and SSS, according to Weiss and Price (1980). P_{atm} was obtained from the National Centers for Environmental Prediction/National Centre for Atmospheric Research (NCEP/NCAR) reanalysis project (Kalnay et al., 1996).

The k_{co2} was calculated as a quadratic function of wind speed (m s^{-1}) updated by Wanninkhof (2014) (Equation (4)) which has a 20% uncertainty:

$$k_{co2}^{sea} = 0.251 U_{10}^{2} \left(\sqrt{\frac{660}{Sc}}\right) \quad (4)$$

where U_{10} is the wind speed (m s^{-1}) at 10 m above the water surface and Sc is the Schmidt dimensionless number determined accordingly to Wanninkhof (2014). Water temperature (for the calculation of Sc) and U_{10} were provided with the SMOS product. To convert partial pressures into molar units, the solubility of CO_2, K_0 (mol L^{-1} atm^{-1}), was calculated according to Weiss (1974). All formulae to calculate K_0, k, Sc and F_{co2}^{sea}, were applied to the SMOS seasonal discharge composites.

The annual net sea-air CO_2 flux (Tg C y^{-1}) refers to the total amount of CO_2 either emitted from the sea to the atmosphere (a positive flux) or taken up by the sea from the atmosphere (a negative flux) in a given year, as calculated by using the molar mass of C, the fraction of a day in a year, and the area of the plume for each SMOS seasonal discharge composite.

2.6. Statistics

The normality of data distribution was tested using the Shapiro-Wilk test. The variance analysis was tested using Kruskal-Wallis for non-parametric data. Tukey's Honest Significance Difference (HSD) post hoc test was conducted to compare differences across the seasons and years. The accuracy of estimates was evaluated using statistical indicators including the coefficient of determination (R^2), root mean square error (RMSE) and the mean relative difference (Bias) expressed respectively as (Eqn 5, 6 and 7):

$$\boldsymbol{R^2} = \frac{\boldsymbol{SS_{res}}}{\boldsymbol{SS_{tot}}} \quad (5)$$

$$\boldsymbol{RMSE} = \sqrt{\frac{\sum_{i=1}^{N} (\boldsymbol{y_i} - \boldsymbol{x_i})^2}{\boldsymbol{N}}} \quad (6)$$

$$\boldsymbol{Bias} = 100.\frac{1}{\boldsymbol{N}} \sum_{i=1}^{N} \frac{\boldsymbol{y_i} - \boldsymbol{x_i}}{\boldsymbol{x_i}} \quad (7)$$

where SS_{res} is the sum of squares of residuals, SS_{tot} is the total sum of squares, x_i is the in situ data for a define parameter and y_i its estimated value.

2.7. Sensitivity analysis

After the adjustment of the multiple polynomial model, a sensitivity analysis (Si) was conducted to identify which model coefficient exerts the most influence on the model results. A sensitivity index comparing changes in the simulated values against changes in the model coefficient was computed to assess the Si (Equation (8)) (Smith and Smith 2007):

$$Si = \frac{(Max\ (P_i) - Min(P_i)}{Max\ (P_i)} \quad (8)$$

where P_i is each model coefficient. After obtaining S_i values, a standardization [$0 \leq S_i \leq 1$] was carried out to compare their relative proportions [S_i /$S_i$max] on the model response.

2.8. Amazon River plume area

Using SSS from SMOS, the area of the ARP was delimited and computed by using a threshold algorithm to map water masses with SSS <35 in the WTNA. The computing was performed using QGIS v.2.18.12 software.

3. Results

3.1. Remote sensing SST and SSS variability

SMOS SST quarterly (3-month) mean images showed the presence of relatively colder (~27 °C) waters during the rising season in the WTNA region, being transported by the NBC along the north coast of Brazil in the direction of the Guianas (Fig. 2). These waters of the ARP had high variation in SSS during the rising season, except for the year of 2013 (Table A2). During the high water season, SST started to increase in the ARP due to the major discharge of warmer waters from the Amazon River (Varona et al., 2019). The position of the ITCZ during the high-falling water season (boreal spring-summer) can alter net heat flux and wind fields in the study area, leading to warmer conditions on the surface (Fournier et al., 2017). SMOS SST are consistent with temperature measurements reported by Lefèvre et al. (2017), with values ranging from 27.8° to 29.5 °C. Although SST in the ARP is generally higher than in the surrounding area, during the falling and low water of 2014, SST in the plume was lower than in the rest of the WTNA.

The opposite trend during the falling and low water of 2010 was observed, where SST in the ARP was much higher (>29 °C) than in the following years. According to Fournier et al. (2017), the area considered as ARP received a greater contribution from the Orinoco River waters in 2010, in comparison to 2011–2014. This interannual difference supports the concept of the influence of climatic variability, for instance the El Niño event in 2010 (Marengo et al., 2011), not only on the Amazon but also in other rivers, such as the Orinoco. The climatic variability was reflected in the record flood in 2014 in the Amazon River basin (Espinoza et al., 2014; Marengo and Espinoza 2016).

The spread of riverine waters in the plume was indicated by a delimited area with SSS <35. The falling water season expressed the largest plume area, significantly different from the rising and low water season (mean falling water season plume area = 11.2 × 10^5 km^2, Kruskal-Wallis $p < 0.05$, Tukey HSD for comparison across seasons, Fig. 3) and SST reached its maximum (~29 °C, Table A3). During the low water season, the plume started to shrink with high values of SST and SSS, the latter parameter with a significant statistical difference between the low water season and the rising and high water seasons (Kruskal-Wallis, $p < 0.05$, Tukey HSD for comparison across seasons), illustrating the mixing of oceanic and riverine waters (Table A2 and Table A3). In all seasons, a zonal area south of the Amazon River mouth shows SSS values (>35) characteristic of oceanic waters in agreement with previous reports. Lentz and Limeburner (1995) observed that the ARP does not extend southeastward beyond the Tocantins River mouth (see Fig. 1).

In spite of the drought of 2010 and the flood of 2012–2014, interannual differences in the plume area (Fig. 3) were not statistically significant (Kruskal-Wallis, $p > 0.05$). Therefore, based in this study results, climatic events were not associated with were notass an observable effect on the spread of the ARP. Instead, the slightly higher areas of 2011 are related to weaker trade winds due to the positioning of the ITZC, which allowed for greater offshore northward advection of the ARP (Fournier et al., 2017).

3.2. Correlation among measured parameters in the ARP and validation of modeled pCO_2

The correlation between in situ SSS and SST with in situ pCO_2 in the study area showed a positive relationship ($N = 15{,}392$, $R^2 = 0.76$, $p < 0.005$, RMSE = 51.95 µatm) (Figure A2). The pCO_2 in situ transects data are shown in Figure A1. To match the SMOS pixel spatial resolution of 0.5°, in situ data were averaged and after a Cook's analysis, outliers were discarded. Basic statistics calculated before and after the averaging are shown in Table A4. The coefficient of variation shows consistency of SSS, SST and pCO_2 values within each pixel (Table A4).

The SSS_i and SST_i values used to generate the model are linearly

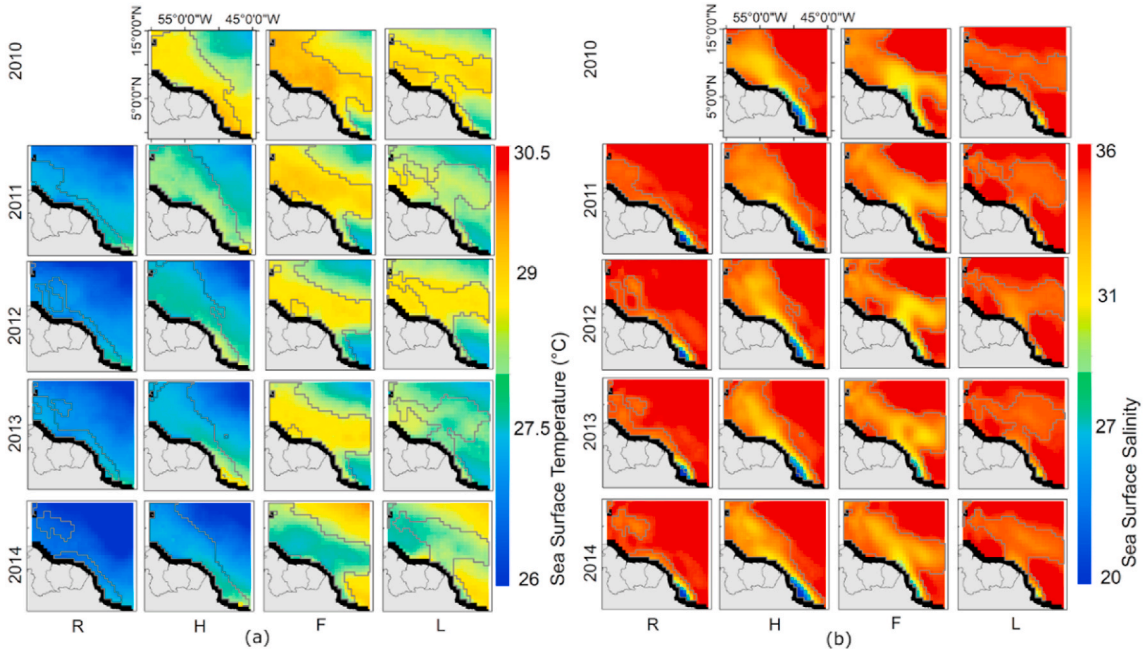

Fig. 2. SMOS Sea Surface Temperature (a) and Sea Surface Salinity (b) for the Western Tropical North Atlantic area, according to the net discharge season: R (Rising: Jan–Mar), H (High: Apr–Jun), F (Falling: Jul–Sep) and L water (Low: Oct–Dec) for 2010–2014. The gray line refers to the ARP (SSS < 35) and the black area refers to no-data (maximum distance of 100 km from the coast). The rising water season of 2010 was not represented in our spatial analyses because SMOS mission only began providing data in May of 2010.

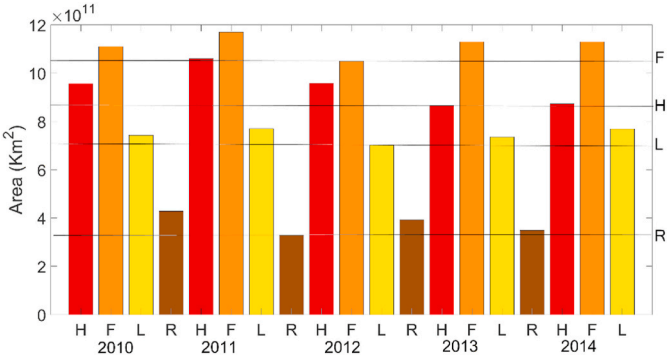

Fig. 3. Computed area for the Amazon River plume by net discharge season from 2010 to 2014. The black lines correspond to the lower area of each season, named on the right side where F, H, L and R goes by Falling, High, Low and Rising season, respectively.

correlated to SSS_{SMOS} and SST_{SMOS} (Fig. 4(a) and (b), respectively). SSS_{SMOS} tends to overestimate in situ SSS for values < 30, while SST_{SMOS} has an underestimate bias of the in situ SST. Reul et al. (2012) also observed an SSS bias where SMOS data are too salty in coastal waters with in situ salinity below 33.

By applying the multiple polynomial regression to SMOS-derived SSS and SST, the empirical function to estimate pCO_2 was derived as follows (Equation (9)):

$$pCO_2 = a\,(SSS)^2 + b(SST)^2 + c(SSS * SST) + d - e(SSS) - f(SST) \quad (9)$$

where a = 0.05; b = 34.81; c = 19.71; d = 48792.07; e = 560.47; f = 2694.56.

The empirical model (Equation (9)) was validated with an independent dataset (Fig. 5(a), N = 76, R^2 = 0.74, RMSE = 30 µatm, Bias = −1.3, p < 0.005), although we have identified an underestimation of values below 300 µatm pCO_2 values < 300 µatm were correlated with salinity <30 (Figure A3) and as shown previously, SMOS has limitations for estimating SSS below this threshold. Nevertheless, we consider the model suitable for representing the pCO_2 distribution throughout ARP with these caveats in mind (Fig. 5(b)). The in situ data used for the comparison between the predicted pCO_2 and in situ pCO_2 (Fig. 5(b)) was the same data used for model validation in which 61% of the dataset corresponded to falling water season, 36% and 4% to high and low water season, respectively. Validation stations are shown in Fig. 1(a). The pCO_2 overestimation observed in higher latitudes (>11.5°N, Fig. 5(b)) is likely related to an underestimation of remotely sensed SST. The underestimation in lower latitudes (<7°N, Fig. 5(b)) was likely related to SSS bias (Fig. 4). More details of this uncertainty analysis are shown in Figure A4.

3.3. Sensitivity analysis

Each coefficient of the model (Equation (9)) was modified in ±5% steps to cover a range of ±20%. The changes in each input into the model varied according to the temperature (i.e. each coefficient in Equation (9) was changed starting with −20% of its original value up to +20% for every fixed temperature from 26 °C up to 30 °C). The maximum sensitivity index reached was reported as the coefficient "e" (SSS) for 26 °C (S_i = 8.93, Table A5) with a maximum value of 100% being attributed. All of the other absolute values of S_i were related to this maximum, resulting in the values presented in Table 2.

The coefficient "e" is the most sensitive followed by the coefficients "a" and "f". The coefficient "e" represents SSS in Equation (9) and according to our analysis, is more sensitive for lower temperatures (26–28 °C). The coefficients "a" and "f" were sensitive only when the temperature reached 30 °C, but such temperatures were not registered by the SMOS SST product used in this study (SST ≤ 29.71, see Table A3). The interval of 26–28 °C is observed predominately during the rising season for all study period. This range is also characteristic of oceanic waters observed in Figure A5.

3.4. Spatiotemporal distribution of pCO_2 and CO_2 fluxes in the ARP

The derived pCO_2 function (Equation (9)) was applied to quarterly

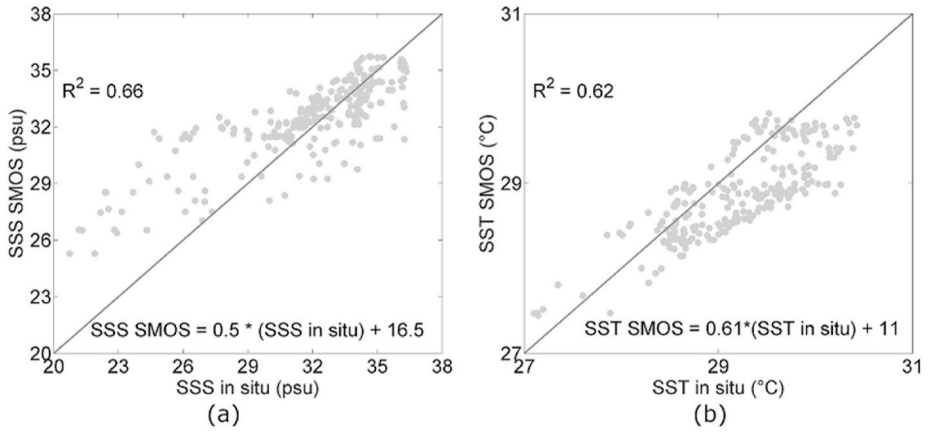

Fig. 4. Linear relationship between: a) in situ SSS_i and SSS_{SMOS} (N = 176, $R^2 = 0.66$, RMSE = 1.23, Bias = 2.6, $p < 0.005$); b) SST_i and $SMOS_{SST}$ (N = 176, $R^2 = 0.62$, RMSE = 0.31 °C, Bias = −1.1; $p < 0.005$).

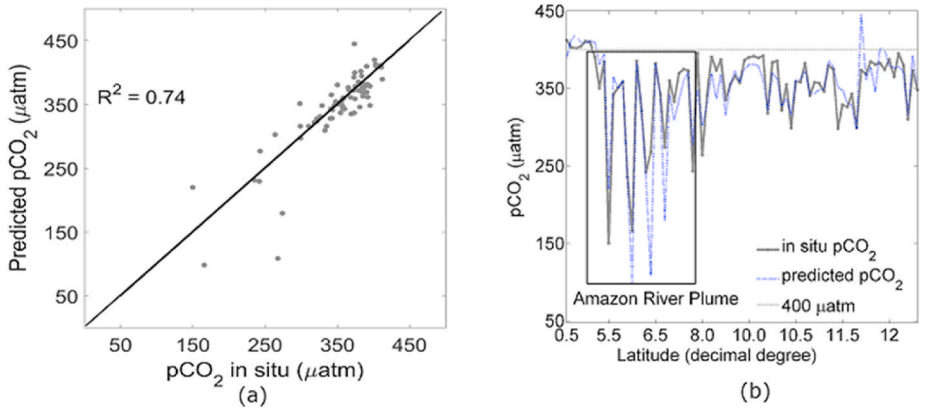

Fig. 5. (a) Validation of the multiple polynomial regression function of SMOS-derived SSS and SST to estimate pCO_2 at the Amazon River plume (N = 76, $R^2 = 0.74$, RMSE = 30 µatm, Bias = −1.3, $p < 0.005$); (b) Latitudinal distribution of in situ pCO_2 and estimated-pCO_2 for the Western Tropical North Atlantic area using SMOS products.

Table 2
Relative sensitivity index values used to evaluate the sensitivity of Equation (9) coefficients to SST (°C) in the Amazon River plume.

Coefficients	Sensitivity Index by Temperature					
	26 °C	27 °C	28 °C	29 °C	30 °C	
a	7	6	3	6		12
b	5	5	5	5	5	
c	5	5	5	5	5	
d	–	–	–	–	–	
e	**100**	65	19	10	12	
f	7	6	2	6	12	

composites of SMOS products, grouped according to the seasonal discharge of the Amazon River (Fig. 6). The estimated-pCO_2 in the ARP ranged between 65 and 841 µatm (µ = 406 ± 24 µatm) during the five-year study period (Table A5), and the rising water season from all years (2011–2014) and the high water season of 2012–2014 presented higher values in comparison to other seasons.

From the pCO_2 distributions, monthly sea-air CO_2 fluxes were calculated for the ARP ranging from −17.55 mmol m^2 d^{-1} during the high water period of 2010, to 43.50 mmol m^2 d^{-1} during the rising water period of 2014 (Table A6). During the rising water season, the ARP was a source of CO_2 to the atmosphere (red colour), likely due to the imprisonment of the CO_2-rich Amazon River water that was trapped against the coast (Fig. 7). During the rest of the seasons (except in 2010), even within the ARP, patches acted as a source of CO_2.

These year to year differences in annual net sea-air CO_2 fluxes (e.g., 2010 was a net sink, whereas 2014 was the largest net source; Fig. 8), was statistically significant for rising and high water seasons (Kruskal-Wallis, $p < 0.05$). The Tukey HSD post-hoc test revealed that F_{co2}^{sea} from the year of 2010 and 2014 had means significantly different for the high water season as well as F_{co2}^{sea} from the rising water season from 2011 to 2014. These pronounced interannual differences, especially 2010 (and 2011) from 2014 indicate the impact of climate variability on the ARP CO_2 balance.

The annual net sea-air flux of CO_2 for the entire plume during the study period (2010–2014) was 5.6 ± 7.2 Tg C y^{-1}, with a significant intra-annual variability (Table 3). If we only consider 2011–2014 since we do not have data for the rising water season of 2010, the annual net sea-air flux of CO_2 increases to 8.6 ± 7.1 Tg C y^{-1}.

4. Discussion

4.1. Spatial trends in pCO_2

The results for the ARP presented here are in a general agreement with pCO_2 values derived from other remote sensing studies in coastal areas dominated by rivers, where the mixing between river and oceanic waters decreases pCO_2 values observed in the plume due to rates of biological uptake and degassing that exceed biological and photo-oxidative organic matter decomposition (Lohrenz and Cai 2006; Bai et al., 2015). Besides the thermodynamic change due to the river-sea

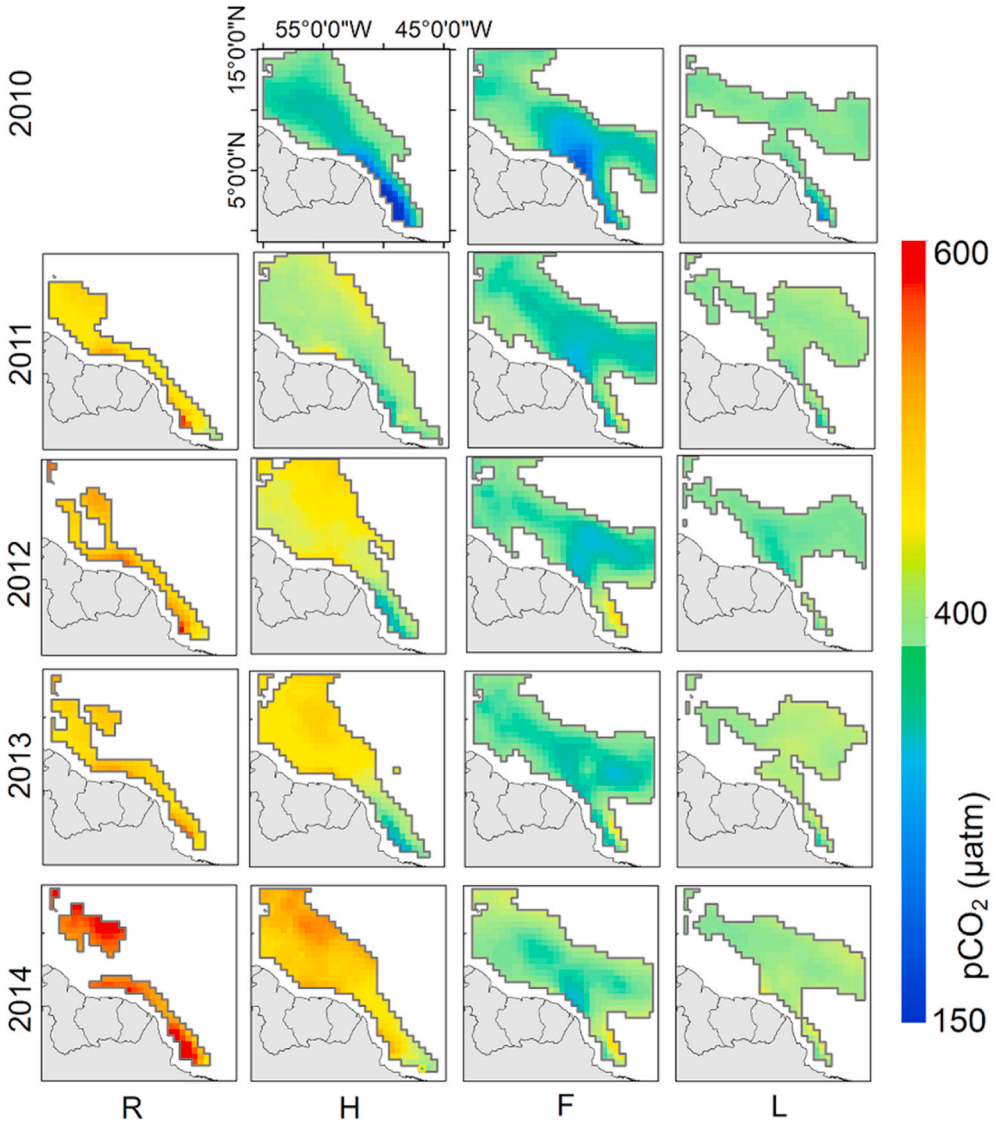

Fig. 6. Estimated-pCO_2 for the Amazon River plume area using SMOS products for the net discharge seasons: R (Rising: Jan–Mar), H (High: Apr–Jun), F (Falling: Jul–Sep) and L water (Low: Oct–Dec) in 2010–2014. The gray line refers to the ARP (SSS < 35). The 100 km close to the coast refers to no-data. The rising water season of 2010 was not represented in our spatial analyses because SMOS mission only began providing data in May of 2010.

water transition and biological uptake, the low buffer capacity of Amazon River water may also result in reduced pCO_2 concentrations when the river meets the sea (Cai et al., 2013). Previous studies described the WTNA area as a source of CO_2 (Takahashi et al., 2009; Landschützer et al., 2014). CO_2 oversaturation in coastal waters due to riverine carbon input has been reported recently and shows a seasonality dependence (Xue et al., 2016; Lohrenz et al., 2018). Our results showed pronounced seasonal and interannual variability in CO_2 fluxes. The significant interannual variability showed that the lowest fluxes occurred in 2010 during an El Niño event and the highest annual fluxes occurred during record floods in 2014. Interannual variability in global ocean pCO_2 have previously been linked to El Niño events (Liu and Xie; 2017).

The optimal-growth zone of phytoplankton on the Amazon shelf occurs mainly seaward of the high-turbidity plume as well as shoreward of the nutrient-depleted offshore water. DeMaster et al. (1983) and DeMaster et al. (1986) reported that the nutrient uptake happens when the turbidity decreases, and the blooms occurred shoreward of the 33 isohaline. Smith and DeMaster (1996) showed that phytoplankton photosynthesis in waters influenced by the Amazon River is limited by low levels of available subsurface irradiance, particularly in the reaches of the plume closest to the river influence (Medeiros et al., 2015). The CO_2 degassed in the plume is derived from CO_2 advected by the river and the decomposition of river dissolved organic matter by microbes in the river (Ward et al. 2013, 2016) or the very early stages of the plume (Medeiros et al., 2015; Seidel et al., 2015).

Medeiros et al. (2015) and Seidel et al. (2015) assessed the fate of organic matter along the Amazon River continuum, elucidating the processes and their spatial variability in the ARP. Near the mouth, where the water is more brackish with lower light penetration, the predominant process was bacterial remineralization, which releases CO_2 to the water. The nearshore area between Amazon River mouth and the Guianas has been reported as a relevant area of remineralization (Aller and Blair 2006).

4.2. Seasonal variability in pCO_2

For the rising water season, when pCO_2 reaches its highest values, the ARP is typically dominated by "oceanic-like water" with lower temperatures and higher salinities (Fig. 2) in comparison to other seasons. Similarly, during January and March, Lefèvre et al. (2017) observed that the French Guiana shelf was a source of CO_2, with salinities > 34. During

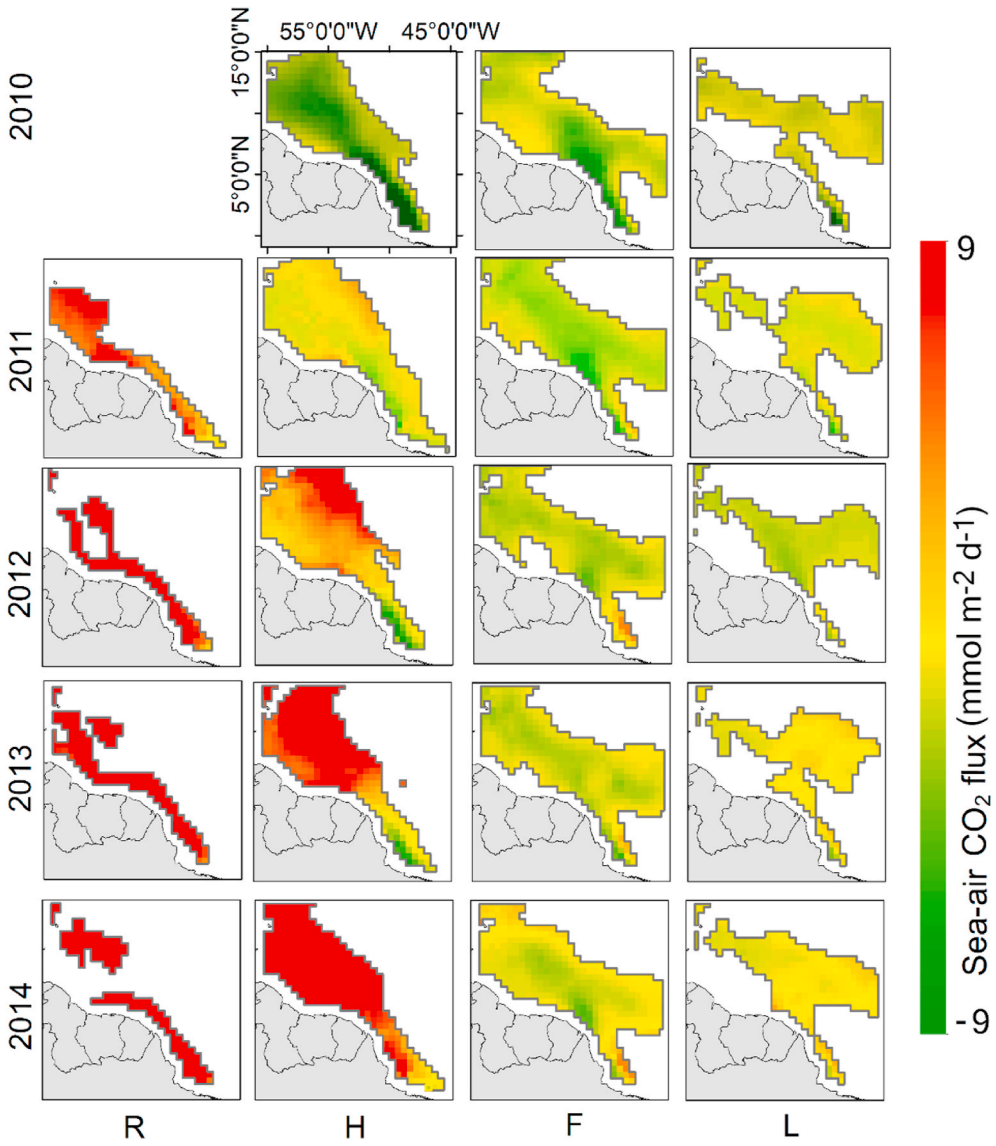

Fig. 7. Sea-air CO_2 flux (mmol m^2 d^{-1}) estimated for the Amazon River plume area with SMOS products for the net discharge seasons: R (Rising: Jan–Mar), H (High: Apr–Jun), F (Falling: Jul–Sep) and L water (Low: Oct–Dec) in 2010–2014. The gray line refers to the ARP (SSS < 35). The 100 km close to the coast refers to no-data. The rising water season of 2010 was not represented in our spatial analyses because SMOS mission only began providing data after May of 2010.

the rising water season, the extent of the ARP is constrained by ocean currents and trade winds. This can promote two situations. The first is that it might decrease the input of nutrients from the river into the ocean. The Amazon River takes about one month from the last discharge measurement station at Óbidos to reach the river mouth, and about two months to reach the distal part of the plume (Hellweger and Gordon 2002; Korosov et al., 2015). This lag indicates that during the rising water season the water that is reaching the outer parts of the ARP may correspond to water discharged from the river during the low water season and have a lower nutrient input than expected. The second situation is that the inner shelf water is less diluted with oceanic waters and is therefore predominantly riverine (lowest values of SSS, see Table A2).

During the high water season, the ARP is driven northwestward by the North Brazil Current, and during the falling water season, a retroflection of the ARP has been observed, driving nutrient-rich waters eastwards (Lentz and Limeburner 1995), leading to lower values of pCO_2 due to biological uptake. Lefèvre et al. (2017) also observed a sink of CO_2 at the French Guiana shelf during the falling water season (August). The overall seasonal pCO_2 values obtained in the present study in the ARP are similar to values previously reported by Cooley et al. (2007) and Ibánhez et al. (2016). However, higher values (>500 μatm) were also observed during the rising water season of 2011 and 2012, and during the rising and high water seasons of 2013 and 2014 (Table A5).

The strongest CO_2 sink observed by Lefèvre et al. (2017) was derived from data acquired on cruises conducted during May and June, which are representative of the high water season. In the case of our study, we observed the largest CO_2 sink during the falling water season. This difference may be due to how we have binned months by season as opposed to the local transect measurements reported by Lefèvre et al. (2017). Lefèvre et al. (2017) sampled during May of 2010 and June of 2011 when our results also indicated that the plume was acting as a CO_2 sink in contrast to the high water seasons from 2012 to 2014, which acted as net CO_2 sources.

4.3. *Influence of extreme climatic events on pCO_2*

The difference in annual CO_2 fluxes from rising and high water seasons during the studied years, especially among the years of 2010 (and 2011) and 2014 show the impact of the extreme climatic events

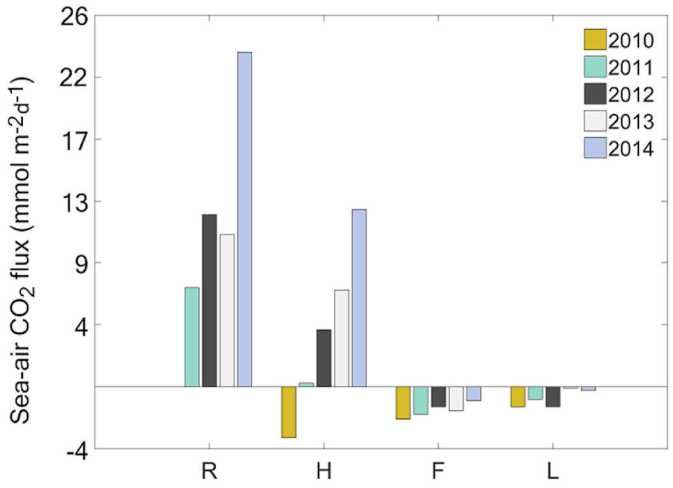

Fig. 8. Average of all sea-air CO_2 flux (mmol m^{-2} d^{-1}) for the Amazon River plume area with SMOS resolution of 0.5° for the net discharge seasons: R (Rising: Jan–Mar), H (High: Apr–Jun), F (Falling: Jul–Sep) and L (Low: Oct–Dec) water in 2010–2014. The rising water season of 2010 was not represented in our spatial analyses because SMOS mission only began providing data in May of 2010.

Table 3
Statistics for the annual net sea-air flux of CO_2 (Tg C y^{-1}) for the Amazon River plume.

Year	Seasonal Discharge	Min	Max	Mean
2010	High	−73.2	−1.9	−15.0 ± 11.5
	Falling	−49	−0.6	−10.9 ± 8.8
	Low	−32.2	−1.4	−4.4 ± 2.9
	All year			−10.1 ± 7.7
2011	Rising	−0.6	25.2	13.0 ± 5.0
	High	−18.8	19	1.1 ± 5.8
	Falling	−39.2	11.1	−9.6 ± 5.8
	Low	−15.9	3.1	−3.0 ± 1.8
	All year			0.4 ± 5.6
2012	Rising	2.5	43.9	17.3 ± 6.1
	High	−25	50.2	16.6 ± 13.9
	Falling	−18.5	21.1	−6.3 ± 5.2
	Low	−8.3	2.6	−4.2 ± 1.4
	All year			5.9 ± 6.6
2013	Rising	7	30.6	18.3 ± 4.4
	High	−24.4	66.8	25.7 ± 17.9
	Falling	−26.8	12.5	−8.0 ± 4.2
	Low	−11.6	6	−0.3 ± .2.7
	All year			8.9 ± 7.3
2014	Rising	7.3	66.2	35.6 ± 9.4
	High	−8.7	85.4	47.2 ± 20.8
	Falling	−23.2	24.7	−4.7 ± 6.7
	Low	−7	10.2	- 1.0 ± 2.8
	All year			19.3 ± 9.9
Average 2010–2014		−19.2	25	5.6 ± 7.2
Average 2011–2014		−13.2	29.9	8.6 ± 7.1

that occurred from 2010 to 2014. The lower outgassing flux from the ARP during the severe drought in 2010 (Marengo et al., 2011) (as shown by the hydrograph, Fig. 1(b)) was likely a consequence of the low discharge of the river to the ocean plus the mixing of riverine-oceanic waters caused by the higher dispersal of the plume associated with weaker trade winds (Fournier et al., 2017). The disconnection of the Amazon River from streams and floodplains due to the unusually low river discharge (Marengo et al., 2011) may explain lower inputs of CO_2 and organic matter to the plume. The effect of the extreme climatic events, especially El Niño, on the connectivity between the hydrological pulse and water quality was also observed by Da Cunha and Sternberg (2018) on estuarine Amazon lakes. The reduced discharge likely resulted in a reduction of turbidity (i.e. lower suspended sediment concentration), allowing more light penetration in the water column that enhances primary production and increases CO_2 uptake.

In contrast, the annual flux of CO_2 during 2012–2014 was positive. This is likely linked to a larger magnitude of CO_2-rich river water discharged to the ARP. Likewise, higher river discharge leads to a greater load of sediment-rich water to the ARP, potentially inhibiting primary production and thereby reducing oceanic CO_2 uptake across a larger swath of the ARP compared to a year with average river discharge. This period was marked by a strong flood that started in 2012 associated with a La Niña event, persisting due to SST anomalies in the Western Tropical Pacific and in the subtropical South Atlantic (Satyamurty et al., 2013; Espinoza et al., 2014; Marengo and Espinoza 2016). During the rising water period of 2014, the rainfall in the southwestern Amazon was 80–100% above normal (Espinoza et al., 2014).

The high rainfall may be responsible for flushing more terrestrial and floodplain material, causing an increase in the input of organic matter and CO_2 from streams and floodplains into the mainstem. For example, Neu et al. (2016) showed that dissolved organic and inorganic carbon fluxes from above ground flow paths (e.g. rainfall, throughfall, stemflow, and overland flow) and stream flow were greater in the Amazon forest during the first large rainfall event after a long dry period. Likewise, Ward et al. (2012) observed a similar phenomenon in streams of the temperate Northwest Pacific in the US, with dissolved organic carbon and vascular plant biomarker (i.e. lignin phenols) concentrations increasing linearly with river discharge during rain events following long dry periods. Additionally, during 2014 the ITCZ was positioned further south compared to its position in 2010, and trade winds were stronger, constraining the ARP closer to the coast (Fournier et al., 2017). These differences between 2010 and 2014 illustrate the dependence of the plume dynamics on large-scale climate patterns.

4.4. CO_2 fluxes

Sea-air CO_2 flux rates obtained in the present study (−17.55 to 43.50 mmol m^2 d^{-1}) are in agreement with values presented by Ibánhez et al. (2015) (−11.00 to 3.70 mmol m^2 d^{-1}). Both results indicate that most of the CO_2 outgassing occurs in lower latitudes and agree that the highest levels of CO_2 outgassing in the ARP occur during the rising water season, whereas the highest levels of CO_2 uptake occur during low water. Integrated across the plume, our results showed a pronounced seasonal and interannual variability (Table A7). Considering the four hydrologic seasons of 2011–2014, the annual net sea-air CO_2 flux from the ARP calculated here (8.6 ± 7.1 Tg C y^{-1}, Table 3) is substantially higher than calculations by Ibánhez et al. (2016) (−7.9 ± 1.0 Tg C y^{-1}). This difference is driven by high fluxes observed during the rising and high water seasons when values as high as 35.6 ± 9.4 Tg C y^{-1} and 47.2 ± 20.8 Tg C y^{-1} were observed in 2014, respectively (Table 3).

This can be explained by: i) climatic events that intensified rainfall in the Amazon River basin during our study period, leading to a higher discharge of river waters into the ocean and; ii) present sampling efforts comprised the entire plume, particularly in areas of the plume closer to the Amazon River mouth. Ibánhez et al. (2016) collected in situ samples to generate the model to estimate pCO_2 in higher latitudes (14°N-5°N; 52°W-41°W) (Ibánhez et al., 2015). In this region, riverine water was more diluted by oceanic waters, supporting phytoplankton blooms that enhance CO_2 uptake. Basing the pCO_2 model only on this region may result in an overestimation of net CO_2 uptake for the whole plume. For example, in the present study, the average minimum carbon flux (i.e., net uptake) we observed was −19 Tg C y^{-1} during the five-year study period (Table 3). In comparison, Subramaniam et al. (2008) estimated that the ARP was on average a net CO_2 sink of 27 Tg C y^{-1} throughout their entire study period.

4.5. Study limitations

The algorithm presented here is based on data acquired by a

microwave orbital sensor that has the advantage of weather independence, in a region where the presence of clouds complicates the application of optical sensors. Although the SMOS sensor has a relatively lower spatial resolution (0.5°) compared to ocean colour sensors operating in the visible part of the electromagnetic spectrum (<4 km), the estimated pCO_2 average values showed a low coefficient of variation within each pixel (Table A4). Despite this, our algorithm had a weak relationship between the range of ~500–750 μatm. This interval speaks for only 3% of our total samples and represents riverine water. Another drawback is that SMOS products are not applicable within 100 km of the coastline due to adjacency effects of land contamination. Considering that ocean currents transport the Amazon River discharge northward along the coast, including this area would likely increase our estimate of CO_2 emissions from the ARP. A limitation faced in our study is the reduced performance of SMOS to retrieve lower values of salinity (<30) (Fig. 4(a)), as SSS error increased when advancing into the river mouth. Part of our in situ salinity samples had to be discarded after an outlier analysis with the SMOS products.

5. Conclusions

The net flux of CO_2 for the Amazon River plume was estimated using remote sensing data and an empirical relationship between in situ pCO_2 and SMOS-derived SSS and SST. SSS was the most important proxy for pCO_2. Results from this study provide increased spatiotemporal coverage of CO_2 fluxes in the ARP when compared with previous studies, particularly in areas closer to the Amazon River mouth. Within the constraints of remote sensors and field measurements, the data and results presented support our hypothesis that inputs of CO_2-rich water from the Amazon River mouth to the ARP, especially during rising and high water, are high enough to offset uptake of CO_2 in the outer plume. Including areas closer to the coastline in the calculation resulted in an annual net sea-air CO_2 flux of 8.6 ± 7.1 Tg C y^{-1}, while previous studies report the ARP as a net CO_2 sink. Our study does not include the nearshore area within 100 km from the coastline due to SMOS constraints; including this area where the river's discharge is primarily transported by ocean currents may further increase our estimates of CO_2 emissions *vs.* uptake.

The impact of large-scale climatic patterns and the hydrological behaviour of the Amazon River on carbon cycling across the river to ocean continuum in the world's largest river system is discussed. The two climatic extremes that occurred during the five-year study period, the record drought of 2010 and floods of 2012–2014, showed an impact on F^{sea}_{co2}, with statistically significant differences.

Future studies require not only additional in situ measurements closer to the coastline and to the Amazon River mouth for algorithm validation, but also, the potential use of an ocean colour remote sensor (s) that would enable a more diverse combination of ocean colour products in relation to pCO_2 estimation, such as CDOM and Chl-a. Such an approach would allow both the coastal and lower river areas to be resolved in concert.

Declaration of competing interest

The authors declare that they have no known competing financial interests or personal relationships that could have appeared to influence the work reported in this paper.

Acknowledgments

We thank Patricia Yager from the University of Georgia, for the Amazon River plume data provided and the collaboration in the development of the manuscript. We appreciate the exchange of ideas with João Felipe dos Santos and Marcelo Gomes from the National Institute for Space Research during the development of the manuscript. We would also like to thank the captains, crew, and science team of the R/V Knorr, R/V Melville, and R/V Atlantis for their support to the scientific goals of the ANACONDAS project (Amazon Influences on the Atlantic: Carbon Export from Nitrogen Fixation by Diatom Symbioses). We would also like to thank the Ocean Salinity Expertise Centre (CECOS) of the CNES-IFREMER Centre Aval de Traitemenent des Donnees SMOS (CATDS), at IFREMER (Plouzane, France) for the daily composite, half degree resolution SMOS SSS and the CarbonTracker from NOAA ESRL, USA, for the Barbados Ragged Point atmosphere pCO_2 time-series data. We also would like to thank NASA for the SeaDAS software freely provided. All data is available in the tables, figures, and supporting information. This study was partially supported by the Coordenação de Aperfeiçoamento de Pessoal de Nível Superior - Brazil (CAPES) - Finance Code 001. A.C. was supported by Conselho Nacional de Desenvolvimento Cientifico e Tecnologico (CNPq, 309684/2018-8). This research was also supported by the Gordon and Betty Moore Foundation Marine Microbial Initiative River-Ocean Continuum of the Amazon project (GBMF#2293 and GBMF#2928), the São Paulo Research Foundation (FAPESP 2018/18491-4), and the US National Science Foundation DEB-1754317.

Appendix A

The supporting information presented here consists of detailed tables of our results that are discussed in the text of Materials and Methods in section 2.2, Results in section 3.2, 3.3 and 3.4 and during the Discussion in section 4.2.

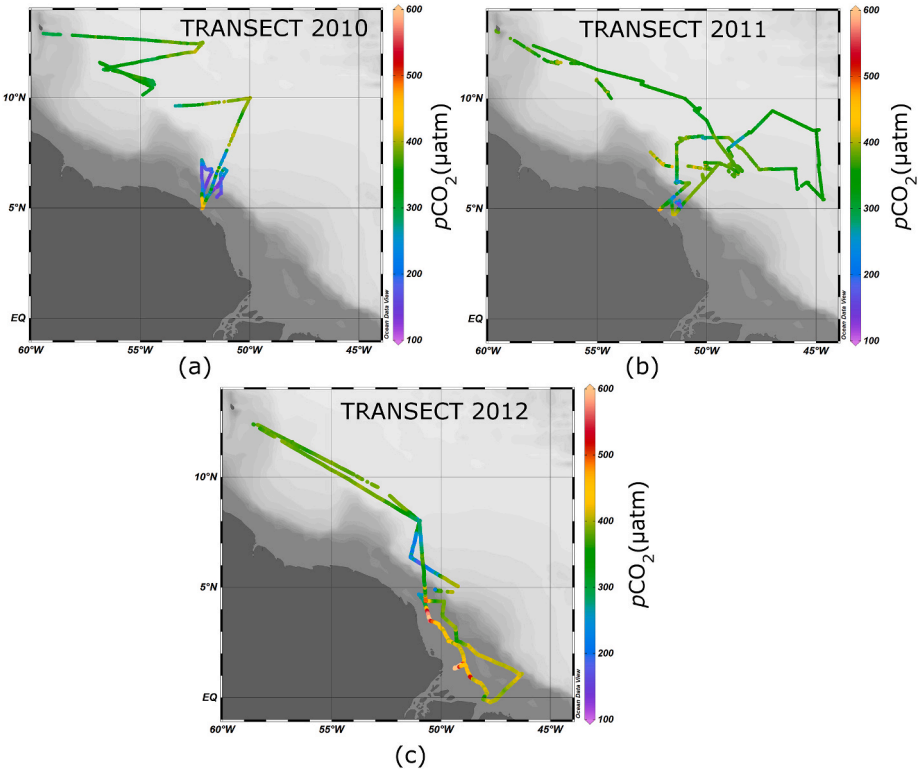

Fig. A1. In situ pCO_2 transects (a) 2010 (b) 2011 (c) 2012.

In situ measurements of SST and SSS had a significant positive correlation with pCO_2 along the oceanographic cruise boundaries (Figure A2(a)) (N = 15,392, R2 = 0.76, p < 0.005, RMSE = 51.95 µatm). In situ pCO_2 ranged between 97 and 976 µatm, while measurements in the WTNA ranged between 120 and 500 µatm (94% of our pCO_2 dataset). These values are similar to measurements shown by Cooley et al. (2007). The weakness of the relationship at the interval 500–750 µatm (high residual values) is likely due to a strong influence of the river. When in situ data from all the three cruises are compiled (Figure A2(b)), two very distinct water masses are observed: river and ocean. Non-linear behaviour of riverine water in both relationships (predicted pCO_2 x in situ pCO_2 and in situ pCO_2 x in situ SSS) was observed. As the samples between 500 and 750 µatm represent only 3% (N = 467) of our total dataset, they do not compromise our overall results.

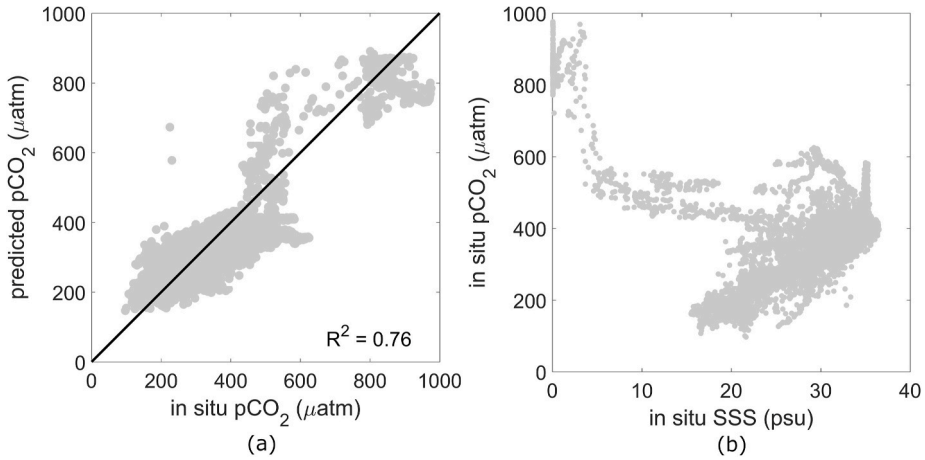

Fig. A2. (a) Multiple polynomial regression between in situ SSS, SST and pCO_2 (N = 15,392, $R^2 = 0.76$, RMSE = 51.95 µatm, p < 0.005; $\boldsymbol{pCO_2} = 0.82\,(\boldsymbol{SSS})^2 + 1.7(\boldsymbol{SST})^2 + 7.7(\boldsymbol{SSS}*\boldsymbol{SST}) + 9770.7 - 262.65(\boldsymbol{SSS}) - 360.14(\boldsymbol{SST})$). (b) Scatter plot of in situ salinity and in situ pCO_2 (2010–2012).

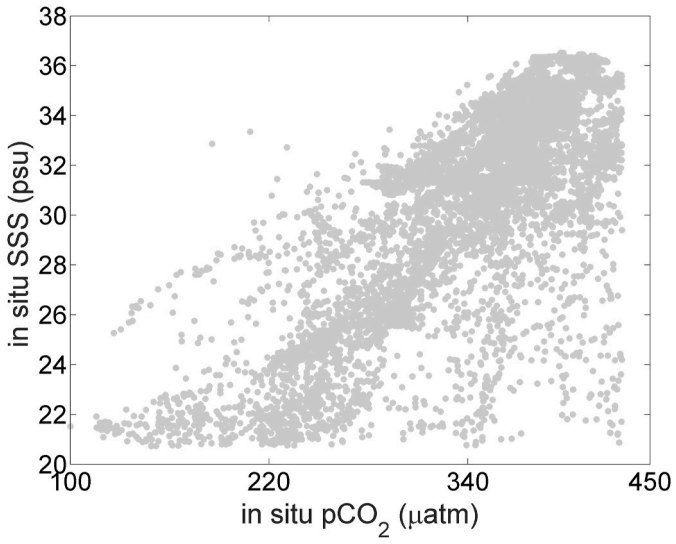

Fig. A3. Correlation between in situ SSS and pCO_2 within the interval of 150–450 μatm (Pearson's correlation, r = 0.78, p < 0.05, N = 13,940).

The pCO_2 deviation was related to SST and SSS bias. SSS is overall overestimated for our study area and SST was underestimated, especially in higher latitudes (>7.5). (Figure A4).

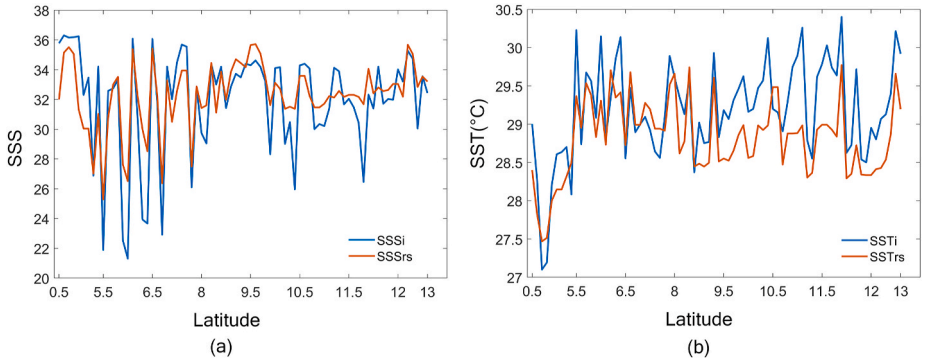

Fig. A4. (a) SSS in situ (SSSi) and SSS SMOS (SSSrs) and (b) SST in situ (SSTi) and SST SMOS (SSTrs) in the study area.

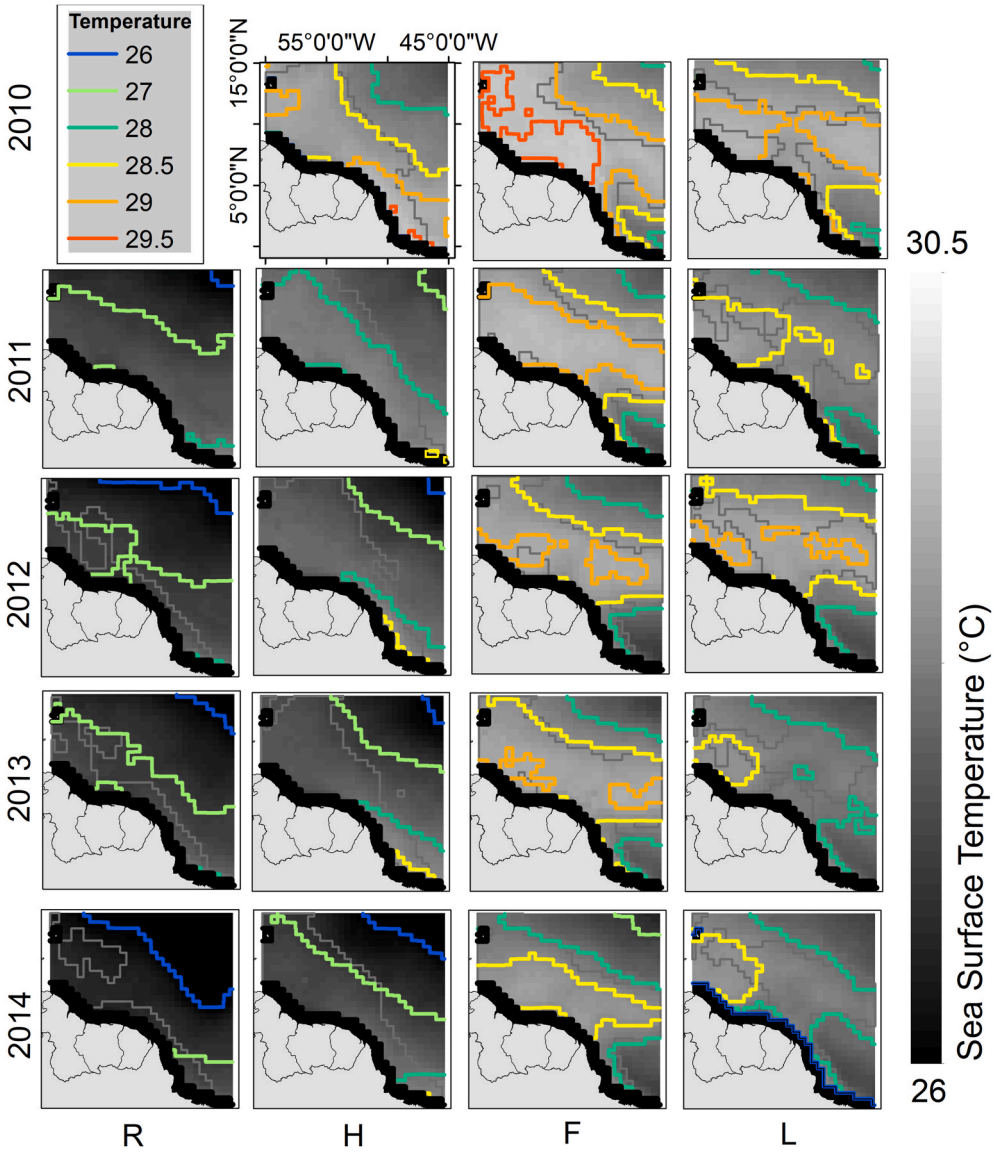

Fig. A5. Contour lines for SST at the Western Tropical North Atlantic. The colored lines refer to the temperature gradient. The gray line refers to the ARP (SSS < 35) and the black area refers to no-data (maximum distance of 100 km from the coast). The rising water season of 2010 was not represented in our spatial analyses because SMOS mission only began providing data after May of 2010.

Although all three cruises crossed the Amazon plume, they had different routes as can be seen in Fig. 1(a). The cruise of 2012 was much closer to the coast and the pCO_2 values are much higher when compared to the other two cruises (Table A1).

Table A1
Basic statistics of in situ pCO_2 sampled during the three oceanographic cruises (2010–2012).

Sampling years of pCO_2 (μatm)	Min	Max	Mean ± Std
2010	97.0	477.0	320.4 ± 76.6
2011	126.3	477.5	349.0 ± 40.6
2012	152.5	976.0	396.45 ± 129.3

Table A2
Statistics for SMOS sea surface salinity - SSS at the Amazon River plume (Std = standard-deviation).

		Min	Max	Mean ± Std
2010	High	20.78	34.99	32.6 ± 2.6
	Falling	26.64	34.99	33 ± 1.7
	Low	27.24	35.00	34.5 ± 0.8
2011	Rising	15.71	34.99	33.6 ± 3.2
	High	20.10	34.99	33.2 ± 2.2
	Falling	26.54	34.98	33.3 ± 1.3

(*continued on next page*)

Table A2 (*continued*)

		Min	Max	Mean ± Std
	Low	30.01	35.00	34.5 ± 0.6
2012	Rising	16.26	34.99	33.3 ± 3.4
	High	20.93	35.00	33.1 ± 2.2
	Falling	26.29	35.00	33.2 ± 1.5
	Low	30.66	35.00	34.4 ± 0.6
2013	Rising	21.65	35.00	33.9 ± 2.2
	High	20.52	34.99	32.9 ± 2.3
	Falling	25.33	35.00	33.3 ± 1.5
	Low	28.49	35.00	34.6 ± 2.8
2014	Rising	14.70	34.97	33.2 ± 3.5
	High	17.93	35.00	32.6 ± 2.8
	Falling	26.09	35.00	33.4 ± 1.5
	Low	27.67	35.00	34.4 ± 0.7

Table A3
Statistics for SMOS sea surface temperature - SST (°C) at the Amazon River plume (Std = standard-deviation).

		Min	Max	Mean ± Std
2010	High	28.35	29.60	28.9 ± 0.2
	Falling	28.30	29.71	29.36 ± 0.2
	Low	28.33	29.28	29.02 ± 0.2
2011	Rising	26.85	28.30	27.46 ± 0.3
	High	27.60	28.60	28.16 ± 0.2
	Falling	27.82	29.43	29.05 ± 0.3
	Low	28.00	28.86	28.43 ± 0.1
2012	Rising	26.46	28.01	27.19 ± 0.3
	High	27.13	28.58	27.81 ± 0.3
	Falling	27.45	29.13	28.76 ± 0.3
	Low	27.86	29.06	28.84 ± 0.2
2013	Rising	26.84	28.06	27.25 ± 0.2
	High	26.82	28.72	27.66 ± 0.4
	Falling	27.72	29.18	28.78 ± 0.2
	Low	27.83	28.61	28.21 ± 0.2
2014	Rising	26.29	27.51	26.75 ± 0.3
	High	26.64	28.51	27.37 ± 0.4
	Falling	27.48	28.87	28.44 ± 0.3
	Low	27.67	28.63	28.26 ± 0.2

Table A4
Statistics and coefficient of variation of the variables used to develop the model for the Amazon River plume, before and after averaging to match the SMOS spatial resolution of 0.5°. The first three parameters (SSS in situ, SST in situ (°C) and pCO_2 in situ (μatm)) (N = 15,392) were measured at surface during three oceanographic cruises and the later three (SSS_i, SST_i (°C) and pCO_{2i} (μatm)) are the parameters subsequent the average to match the SMOS spatial resolution of 0.5° (N = 318).

Variable name	Variable description	Min	Max	Mean	Median	C.V. min (%)	C.V. max (%)	C.V. mean (%)
SSS in situ	In situ sea surface salinity	0.04	36.5	30.2 ± 6.9	32.2	–	–	–
SST in situ (°C)	In situ sea surface temperature	26.9	30.8	29.0 ± 0.7	29.0	–	–	–
pCO_2 in situ (μatm)	In situ sea pCO_2	96.7	976.0	370.6 ± 106.6	372.3	–	–	–
SSS_i	In situ sea surface salinity averaged	20.7	36.3	31.8 ± 3.4	32.5	0.002	20.2	1.6
SST_i (°C)	In situ sea surface temperature averaged	27.1	30.4	29.2 ± 0.6	29.3	0.007	3.5	0.3
pCO_{2i} (μatm)	In situ sea pCO_2 averaged	150.1	433.0	349.1 ± 49.4	360.1	0.03	21.3	2.8

Table A5
Statistics for the estimated pCO_2 (μatm) for the Amazon River plume.

Year	Seasonal Discharge	Min	Max	Mean
2010	High	65.0	380.7	338.2 ± 55.2
	Falling	192.4	384.4	342.0 ± 38.8
	Low	247.5	380.9	369.0 ± 12.9
2011	Rising	382.2	576.3	451.9 ± 27.7
	High	324.6	428.8	389.0 ± 14.2
	Falling	285.4	411.7	353.2 ± 19.8
	Low	338.3	396.5	377.2 ± 6.3
2012	Rising	408.7	599.6	489.8 ± 30.3
	High	313.3	480.0	419.0 ± 27.7
	Falling	302.8	438.8	358.8 ± 22.6
	Low	348.4	404.8	368.3 ± 6.8
2013	Rising	426.8	553.5	474.3 ± 20.3
	High	290.3	509.7	436.8 ± 36.6
	Falling	305.3	422.6	358.2 ± 15.8

(*continued on next page*)

Table A5 (*continued*)

Year	Seasonal Discharge	Min	Max	Mean
	Low	350.2	407.8	386.9 ± 7.7
2014	Rising	440.8	841.2	561.9 ± 49.3
	High	358.1	545.0	479.9 ± 35.5
	Falling	307.9	436.5	373.1 ± 18.0
	Low	367.8	421.2	385.1 ± 8.8
Average 2010–2014				405.9 ± 23.9
Average 2011–2014				416.4 ± 21.7

Table A6
Sensitivity index for each coefficient of the model (a,b,c,d,e,f, Equation (6)), in the interval of 26–30 °C.

Temperature Coefficients	26	27	28	29	30
a	0.62	0.54	−0.31	0.54	**1.03**
b	0.42	0.42	0.42	0.42	0.42
c	0.42	0.42	0.42	0.42	0.42
d	–	–	–	–	–
e	**8.93**	**−5.83**	**−1.74**	−0.85	**1.03**
f	0.61	0.53	0.21	0.54	**1.03**

Table A7
Statistics for the Sea-air CO_2 flux (mmol m^2 d^{-1}) for the Amazon River plume.

Year	Seasonal Discharge	Min	Max	Mean
2010	High	−17.55	−0.46	−3.59 ± 2.76
	Falling	−10.11	−0.13	−2.26 ± 1.82
	Low	−9.93	−0.44	−1.37 ± 0.88
2011	Rising	−0.33	13.47	6.96 ± 2.69
	High	−4.07	4.11	0.23 ± 1.27
	Falling	−7.64	2.17	−1.88 ± 1.14
	Low	−4.73	0.91	−0.90 ± 0.54
2012	Rising	1.77	30.61	12.08 ± 4.28
	High	−5.97	12	3.98 ± 3.31
	Falling	−4.02	4.59	−1.38 ± 1.13
	Low	−2.71	0.84	−1.37 ± 0.46
2013	Rising	4.09	17.83	10.67 ± 2.59
	High	−6.45	17.67	6.79 ± 4.72
	Falling	−5.41	2.53	−1.61 ± 0.84
	Low	−3.62	1.88	−0.10 ± 0.82
2014	Rising	4.80	43.50	23.39 ± 6.20
	High	−2.29	22.4	12.37 ± 5.46
	Falling	−4.69	4.99	−0.95 ± 1.35
	Low	−2.08	3.05	−0.29 ± 0.83
Average 2010–2014				3.39 ± 2.35
Average 2011–2014				4.55 ± 2.45

References

Abril, G., Martinez, J.-M., Artigas, L.F., Moreira-Turcq, P., Benedetti, M.F., Vidal, L., Meziane, T., Kim, J.-H., Bernardes, M.C., Savoye, N., Deborde, J., Souza, E.L., Albéric, P., Landim de Souza, M.F., Roland, F., 2014. Amazon River carbon dioxide outgassing fuelled by wetlands. Nature 505, 395–398. https://doi.org/10.1038/nature12797.

Akuetevi, C.Q.C., Wirth, A., 2015. Dynamics of turbulent western-boundary currents at low latitude in a shallow-water model. Ocean Sci. https://doi.org/10.5194/os-11-471-2015.

Aller, R.C., Blair, N.E., 2006. Carbon remineralization in the Amazon–Guianas tropical mobile mudbelt: a sedimentary incinerator. Continent. Shelf Res. 26, 2241–2259. https://doi.org/10.1016/j.csr.2006.07.016.

Arellano, A.R., Bianchi, T.S., Osburn, C.L., D'Sa, E.J., Ward, N.D., Oviedo-Vargas, D., Joshi, I.D., Ko, D.S., Shields, M.R., Kurian, G., Green, J., 2019. Mechanisms of organic matter export in Estuaries with contrasting carbon sources. J. Geophys. Res. Biogeosciences 1–21. https://doi.org/10.1029/2018jg004868.

Bai, Y., Cai, W.-J., He, X., Zhai, W., Pan, D., Dai, M., Yu, P., 2015. A mechanistic semi-analytical method for remotely sensing sea surface pCO2 in river-dominated coastal oceans: a case study from the East China Sea. J. Geophys. Res. Ocean. 120, 1–19. https://doi.org/10.1002/2014JC010632.

Cai, W.-J., Arthur Chen, C.T., Borges, A., 2013. Carbon dioxide dynamics and fluxes in coastal waters influenced by river plumes. Biogeochem. Dyn. Major River-Coastal Interfaces 155–173. https://doi.org/10.1017/cbo9781139136853.010.

Castelão, G.P., Johns, W.E., 2011. Sea surface structure of North Brazil Current rings derived from shipboard and moored acoustic Doppler current profiler observations. J. Geophys. Res. Ocean. https://doi.org/10.1029/2010JC006575.

Cole, J.J., Prairie, Y.T., Caraco, N.F., McDowell, W.H., Tranvik, L.J., Striegl, R.G., Duarte, C.M., Kortelainen, P., Downing, J.A., Middelburg, J.J., Melack, J., 2007. Plumbing the global carbon cycle: Integrating inland waters into the terrestrial carbon budget. Ecosystems 10, 171–184. https://doi.org/10.1007/s10021-006-9013-8.

Coles, V.J., Brooks, M.T., Hopkins, J., Stukel, M.R., Yager, P.L., Hood, R.R., 2013. The pathways and properties of the Amazon River plume in the Tropical North atlantic ocean. J. Geophys. Res. Ocean. 118, 6894–6913. https://doi.org/10.1002/2013JC008981.

Cooley, S.R., Coles, V.J., Subramaniam, A., Yager, P.L., 2007. Seasonal variations in the Amazon plume-related atmospheric carbon sink. Global Biogeochem. Cycles 21, 1–15. https://doi.org/10.1029/2006GB002831.

Da Cunha, A.C., Sternberg, L. da S.L., 2018. Using stable isotopes 18 O and 2 H of lake water and biogeochemical analysis to identify factors affecting water quality in four estuarine Amazonian shallow lakes. Hydrol. Process. 1–14 https://doi.org/10.1002/hyp.11462.

Dagg, M., Benner, R., Lohrenz, S., Lawrence, D., 2004. Transformation of dissolved and particulate materials on continental shelves influenced by large rivers: plume processes. Continent. Shelf Res. 24, 833–858. https://doi.org/10.1016/j.csr.2004.02.003.

DeMaster, D.J., Knapp, G.B., Nittrouer, C.A., 1983. Biological uptake and accumulation of silica on the Amazon continental shelf. Geochem. Cosmochim. Acta 47, 1713–1723. https://doi.org/10.1016/0016-7037(83)90021-2.

DeMaster, D.J., Kuehl, S.A., Nittrouer, C.A., 1986. Effects of suspended sediments on geochemical processes near the mouth of the Amazon River: examination of biological silica uptake and the fate of particle-reactive elements. Continent. Shelf Res. 6, 107–125. https://doi.org/10.1016/0278-4343(86)90056-7.

Donlon, C.J., Martin, M., Stark, J., Roberts-Jones, J., Fiedler, E., Wimmer, W., 2012. The Operational Sea surface temperature and sea Ice analysis (OSTIA) system. Remote Sens. Environ. https://doi.org/10.1016/j.rse.2010.10.017.

Espinoza, J.C., Marengo, J.A., Ronchail, J., Carpio, J.M., Flores, L.N., Guyot, J.L., 2014. The extreme 2014 flood in south-western Amazon basin: the role of tropical-subtropical South Atlantic SST gradient. Environ. Res. Lett. 9 https://doi.org/10.1088/1748-9326/9/12/124007, 124007.

Fournier, S., Vandemark, D., Gaultier, L., Lee, T., Jonsson, B., Gierach, M.M., 2017. Interannual variation in offshore advection of Amazon-Orinoco plume waters: observations, forcing mechanisms, and impacts. J. Geophys. Res. Ocean. 122, 8966–8982. https://doi.org/10.1002/2017JC013103.

Fratantoni, D.M., Richardson, P.L., 2006. The evolution and demise of North Brazil Current rings. J. Phys. Oceanogr. https://doi.org/10.1175/JPO2907.1.

Garzoli, S.L., Ffield, A., Johns, W.E., Yao, Q., 2004. North Brazil Current retroflection and transports. J. Geophys. Res. Ocean. https://doi.org/10.1029/2003jc001775.

Goes, J.I., Gomes, H.D.R., Chekalyuk, A.M., Carpenter, E.J., Montoya, J.P., Coles, V.J., Yager, P.L., Berelson, W.M., Capone, D.G., Foster, R.a., Steinberg, D.K., Subramaniam, A., Hafez, M.a., 2014. Influence of the Amazon River discharge on the biogeography of phytoplankton communities in the western tropical north Atlantic. Prog. Oceanogr. 120, 29–40. https://doi.org/10.1016/j.pocean.2013.07.010.

Gouveia, N.A., Gherardi, D.F.M., Wagner, F.H., Paes, E.T., Coles, V.J., Aragão, L.E.O.C., 2019. The salinity structure of the Amazon River plume drives spatiotemporal variation of oceanic primary productivity. J. Geophys. Res. Biogeosciences 124, 147–165. https://doi.org/10.1029/2018JG004665.

Grodsky, S.a., Reverdin, G., Carton, J.a., Coles, V.J., 2014. Year-to-year salinity changes in the Amazon plume: contrasting 2011 and 2012 Aquarius/SACD and SMOS satellite data. Remote Sens. Environ. 140, 14–22. https://doi.org/10.1016/j.rse.2013.08.033.

Hales, B., Strutton, P.G., Saraceno, M., Letelier, R., Takahashi, T., Feely, R., Sabine, C., Chavez, F., 2012. Satellite-based prediction of pCO2 in coastal waters of the eastern North Pacific. Prog. Oceanogr. 103, 1–15. https://doi.org/10.1016/j.pocean.2012.03.001.

Hedges, J.I., Keil, R.G., Aransas, P., 1997. What happens to terrestrial organic matter in the ocean? Org. Geochem. 27, 195–212. https://doi.org/10.1016/s0146-6380(97)00066-1.

Hellweger, F.L., Gordon, A.L., 2002. Tracing Amazon River water into the Caribbean Sea. J. Mar. Res. 60, 537–549. https://doi.org/10.1357/002224002762324202.

Ibánhez, J.S.P., Araujo, M., Lefèvre, N., 2016. The overlooked tropical oceanic CO2 sink. Geophys. Res. Lett. 43, 3804–3812. https://doi.org/10.1002/2016GL068020.

Ibánhez, J.S.P., Diverrès, D., Araujo, M., Lefèvre, N., 2015. Seasonal and interannual variability of sea-air CO 2 fluxes in the tropical Atlantic affected by the Amazon River plume. Global Biogeochem. Cycles 28, 1–16. https://doi.org/10.1002/2015GB005110.

Johns, W.E., Lee, T.N., Beardsley, R.C., Candela, J., Limeburner, R., Castro, B., 1998. Annual cycle and variability of the north Brazil current. J. Phys. Oceanogr. 28, 103–128. https://doi.org/10.1175/1520-0485(1998)028<0103:ACAVOT>2.0.CO;2.

Joshi, I.D., Ward, N.D., D'Sa, E.J., Osburn, C.L., Bianchi, T.S., Oviedo-Vargas, D., 2018. Seasonal trends in surface pCO_2 and air-sea CO_2 fluxes in Apalachicola Bay, Florida, from VIIRS ocean color. J. Geophys. Res. B 123 (8), 2466–2484. https://doi.org/10.1029/2018JG004391.

Kalnay, E., Kanamitsu, M., Kistler, R., Collins, W., Deaven, D., Gandin, L., Iredell, M., Saha, S., White, G., Woollen, J., Zhu, Y., Chelliah, M., Ebisuzaki, W., Higgins, W., Janowiak, J., Mo, K.C., Ropelewski, C., Wang, J., Leetmaa, A., Reynolds, R., Jenne, R., Joseph, D., 1996. The NCEP/NCAR 40-year reanalysis project. Bull. Am. Meteorol. Soc. 437–471.

Korosov, A., Counillon, F., Johannessen, J.A., 2015. Monitoring the spreading of the Amazon freshwater plume by MODIS, SMOS, Aquarius, and TOPAZ. J. Geophys. Res. C Oceans 120, 268–283. https://doi.org/10.1002/2014JC010155.

Land, P.E., Findlay, H.S., Shutler, J.D., Ashton, I.G.C., Holding, T., Grouazel, A., Girard-Ardhuin, F., Reul, N., Piolle, J.F., Chapron, B., Quilfen, Y., Bellerby, R.G.J., Bhadury, P., Salisbury, J., Vandemark, D., Sabia, R., 2019. Optimum satellite remote sensing of the marine carbonate system using empirical algorithms in the global ocean, the Greater Caribbean, the Amazon Plume and the Bay of Bengal. Remote Sens. Environ. 235 https://doi.org/10.1016/j.rse.2019.111469, 111469.

Landschützer, P., Gruber, N., Bakker, D.C.E., Schuster, U., 2014. Recent variability of the global ocean carbon sink. Global Planet. Change 927–949. https://doi.org/10.1002/2014GB004853 (Received).

Lefévre, N., Diverrés, D., Gallois, F., 2010. Origin of CO2 undersaturation in the western tropical Atlantic. Tellus Ser. B Chem. Phys. Meteorol. 62, 595–607. https://doi.org/10.1111/j.1600-0889.2010.00475.x.

Lefèvre, N., Flores Montes, M., Gaspar, F.L., Rocha, C., Jiang, S., De Araújo, M.C., Ibánhez, J.S.P., 2017. Net heterotrophy in the Amazon continental shelf changes rapidly to a sink of CO2 in the outer Amazon plume. Front. Mar. Sci. 4 https://doi.org/10.3389/fmars.2017.00278.

Lentz, S.J., Limeburner, R., 1995. The Amazon River plume during AMASSEDS: subtidal current variability and the importance of wind forcing. J. Geophys. Res. 100, 2355–2375. https://doi.org/10.1029/94JC01411.

Liu, W.T., Xie, X., 2017. Space observation of carbon dioxide partial pressure at ocean surface. IEEE J. Sel. Top. Appl. Earth Obs. Remote Sens. 10, 5472–5484. https://doi.org/10.1109/JSTARS.2017.2766138.

Lohrenz, S.E., Cai, W.-J., 2006. Satellite ocean color assessment of air-sea fluxes of CO2 in a river-dominated coastal margin. Geophys. Res. Lett. 33 https://doi.org/10.1029/2005GL023942. L01601.

Lohrenz, S.E., Cai, W.J., Chakraborty, S., Huang, W.J., Guo, X., He, R., Xue, Z., Fennel, K., Howden, S., Tian, H., 2018. Satellite estimation of coastal pCO2and air-sea flux of carbon dioxide in the northern Gulf of Mexico. Remote Sens. Environ. 207, 71–83. https://doi.org/10.1016/j.rse.2017.12.039.

Marengo, J.A., Espinoza, J.C., 2016. Extreme seasonal droughts and floods in Amazonia: causes, trends and impacts. Int. J. Climatol. 36, 1033–1050. https://doi.org/10.1002/joc.4420.

Marengo, J.A., Tomasella, J., Alves, L.M., Soares, W.R., Rodriguez, D.A., 2011. The drought of 2010 in the context of historical droughts in the Amazon region. Geophys. Res. Lett. 38, 1–5. https://doi.org/10.1029/2011GL047436.

Mecklenburg, S., Drusch, M., Kerr, Y.H., Font, J., Martin-Neira, M., Delwart, S., Buenadicha, G., Reul, N., Daganzo-Eusebio, E., Oliva, R., Crapolicchio, R., 2012. ESA's soil moisture and ocean salinity mission: mission performance and operations. IEEE Trans. Geosci. Rem. Sens. 50, 1354–1366. https://doi.org/10.1109/TGRS.2012.2187666.

Medeiros, P.M., Seidel, M., Ward, N.D., Carpenter, E.J., Gomes, H.R., Niggemann, J., Krusche, A.V., Richey, J.E., Yager, P.L., Dittmar, T., 2015. Fate of the Amazon River dissolved organic matter in the tropical atlantic ocean. Global Biogeochem. Cycles 29, 1–14. https://doi.org/10.1002/2015GB005115.

Melack, J.M., 2016. Aquatic Ecosystems. In: Nagy, L., et al. (Eds.), Interactions between Biosphere, Atmosphere and Human Land Use in the Amazon Basin, Ecological Studies, vol. 227. Springer-Verlag Berlin Heidelberg. https://doi.org/10.1007/978-3-662-49902-3.

Molleri, G.S.F., Novo, E.M.L.d.M., Kampel, M., 2010. Space-time variability of the Amazon River plume based on satellite ocean color. Continent. Shelf Res. 30, 342–352. https://doi.org/10.1016/j.csr.2009.11.015.

Müller-Karger, F.E., McClain, C.R., Fisher, T.R., Esaias, W.E., Varela, R., 1989. Pigment distribution in the Caribbean sea: observations from space. Prog. Oceanogr. https://doi.org/10.1016/0079-6611(89)90024-4.

Muller-Karger, F.E., McClain, C.R., Richardson, P.L., 1988. The dispersal of the Amazon's water. Nature. https://doi.org/10.1038/333056a0.

Neu, V., Ward, N.D., Krusche, A.V., Neill, C., 2016. Dissolved organic and inorganic carbon flow paths in an Amazonian transitional forest. Front. Mar. Sci. 3 https://doi.org/10.3389/fmars.2016.00114.

Raymond, P.A., Hartmann, J., Lauerwald, R., Sobek, S., McDonald, C.P., Hoover, M., Butman, D., Striegl, R., Mayorga, E., Humborg, C., Kortelainen, P., Durr, H., Meybeck, M., Ciais, P., Guth, P., 2013. Global carbon dioxide emissions from inland waters. Nature 503, 355–359. https://doi.org/10.1038/nature12760.

Reul, N., Tenerelli, J., Boutin, J., Chapron, B., Paul, F., Brion, E., Gaillard, F., Archer, O., 2012. Overview of the first SMOS sea surface salinity products. Part I: quality assessment for the second half of 2010. IEEE Trans. Geosci. Rem. Sens. 50, 1636–1647. https://doi.org/10.1109/TGRS.2012.2188408.

Richardson, P.L., Hufford, G.E., Limeburner, R., 1994. North Brazil Current retroflection eddies. J. Geophys. Res. https://doi.org/10.1029/93JC03486.

Richey, J.E., Hedges, J.I., Devol, A.H., Quay, P.D., Victoria, R., Martinelli, L., Forsberg, B.R., 1990. Biogeochemistry of carbon in the Amazon River. Limnol. Oceanogr. 35, 352–371.

Richey, J.E., Melack, J.M., Aufdenkampe, A.K., Ballester, V.M., Hess, L.L., 2002. Outgassing from Amazonian rivers and wetlands as a large tropical source of atmospheric CO2. Nature 416, 617–620. https://doi.org/10.1038/416617a.

Rödenbeck, C., Bakker, D.C.E., Gruber, N., Iida, Y., Jacobson, A.R., Jones, S., Landschützer, P., Metzl, N., Nakaoka, S., Olsen, A., Park, G.H., Peylin, P., Rodgers, K.B., Sasse, T.P., Schuster, U., Shutler, J.D., Valsala, V., Wanninkhof, R., Zeng, J., 2015. Data-based estimates of the ocean carbon sink variability - first results of the Surface Ocean pCO2 Mapping intercomparison (SOCOM). Biogeosciences 12, 7251–7278. https://doi.org/10.5194/bg-12-7251-2015.

Salisbury, J., Vandemark, D., Campbell, J., Hunt, C., Wisser, D., Reul, N., Chapron, B., 2011. Spatial and temporal coherence between Amazon River discharge, salinity, and light absorption by colored organic carbon in western tropical Atlantic surface waters. J. Geophys. Res. 116, 1–14. https://doi.org/10.1029/2011JC006989.

Satyamurty, P., Da Costa, C.P.W., Manzi, A.O., Candido, L.A., 2013. A quick look at the 2012 record flood in the Amazon Basin. Geophys. Res. Lett. 40, 1396–1401. https://doi.org/10.1002/grl.50245.

Sawakuchi, H.O., Neu, V., Ward, N.D., Barros, M.D.L.C., Valerio, A., Gagne-maynard, W., Cunha, A.C., Fernanda, D., Diniz, J.E., Brito, D.C., Krusche, A.V., Richey, J.E., 2017. Carbon dioxide emissions along the lower Amazon River. Front. Mar. Sci. 4, 1–12. https://doi.org/10.3389/fmars.2017.00076.

Seidel, M., Yager, P.L., Ward, N.D., Carpenter, E.J., Gomes, H.R., Krusche, A.V., Richey, J.E., Dittmar, T., Medeiros, P.M., 2015. Molecular-level changes of dissolved organic matter along the Amazon River-to-ocean continuum. Mar. Chem. 177, 218–231. https://doi.org/10.1016/j.marchem.2015.06.019.

Signorini, S.R., Mannino, A., Najjar Jr., R.G., Friedrichs, M.A.M., Cai, W., Salisbury, J., Wang, Z.A., Thomas, H., Shadwick, E., 2013. Surface ocean p CO 2 seasonality and sea-air CO 2 flux estimates for the North American east coast. J. Geophys. Res. 118, 5439–5460. https://doi.org/10.1002/jgrc.20369.

Smith, J., Smith, P., 2007. Environmental Modelling: an Introduction. Oxford University Press.

Smith, W.O., DeMaster, D.J., 1996. Phytoplankton biomass and productivity in the Amazon River plume: correlation with seasonal river discharge. Continent. Shelf Res. 16, 291–319. https://doi.org/10.1016/0278-4343(95)00007-N.

Song, X., Bai, Y., Cai, W.J., Arthur Chen, C.T., Pan, D., He, X., Zhu, Q., 2016. Remote sensing of sea surface pCO2in the Bering sea in summer based on a mechanistic semi-analytical algorithm (MeSAA). Rem. Sens. 8, 1–25. https://doi.org/10.3390/rs8070558.

Subramaniam, A., Yager, P.L., Carpenter, E.J., Mahaffey, C., Björkman, K., Cooley, S., Kustka, A.B., Montoya, J.P., Sañudo-Wilhelmy, S.A., Shipe, R., Capone, D.G., 2008. Amazon River enhances diazotrophy and carbon sequestration in the tropical North

Atlantic Ocean. Proc. Natl. Acad. Sci. U. S. A 105, 10460–10465. https://doi.org/10.1073/pnas.0710279105.

Takahashi, T., Sutherland, S.C., Wanninkhof, R., Sweeney, C., Feely, R.A., Chipman, D. W., Hales, B., Friederich, G., Chavez, F., Sabine, C., Watson, A., Bakker, D.C.E., Schuster, U., Metzl, N., Yoshikawa-Inoue, H., Ishii, M., Midorikawa, T., Nojiri, Y., Krtzinger, A., Steinhoff, T., Hoppema, M., Olafsson, J., Arnarson, T.S., Tilbrook, B., Johannessen, T., Olsen, A., Bellerby, R., Wong, C.S., Delille, B., Bates, N.R., Baar, H. J.W., 2009. Climatological mean and decadal change in surface ocean pCO2, and net sea-air CO2 flux over the global oceans. Deep. Res. Part II Top. Stud. Oceanogr. 56, 554–577. https://doi.org/10.1016/j.dsr2.2008.12.009.

Talone, M., Camps, A., Mourre, B., Sabia, R., Vall-Llossera, M., Gourrion, J., Gabarró, C., Font, J., 2009. Simulated SMOS levels 2 and 3 products: the effect of introducing argo data in the processing chain and its impact on the error induced by the vicinity of the coast. IEEE Trans. Geosci. Rem. Sens. https://doi.org/10.1109/TGRS.2008.2011618.

Telszewski, M., Chazottes, A., Schuster, U., Watson, A.J., Moulin, C., Bakker, D.C.E., Gonz, M., 2009. Estimating the monthly pCO2 distribution in the North Atlantic using a self-organizing neural network. Biogeosciences 6, 1405–1421.

Ternon, J., Oudot, C., Dessier, A., Diverres, D., 2000. A seasonal tropical sink for atmospheric CO2 in the Atlantic ocean: the role of the Amazon River discharge. Mar. Chem. 68, 183–201. https://doi.org/10.1016/S0304-4203(99)00077-8.

Tranvik, L.J., Downing, J.A., Cotner, J.B., Loiselle, S.A., Striegl, R.G., Ballatore, T.J., Dillon, P., Finlay, K., Fortino, K., Knoll, L.B., 2009. Lakes and reservoirs as regulators of carbon cycling and climate. Limnol. Oceanogr. 54, 2298–2314. https://doi.org/10.4319/lo.2009.54.6_part_2.2298.

Varona, H.L., Veleda, D., Silva, M., Cintra, M., Araujo, M., 2019. Amazon River plume influence on western tropical atlantic dynamic variability. Dynam. Atmos. Oceans 85, 1–15. https://doi.org/10.1016/j.dynatmoce.2018.10.002.

Wanninkhof, R., 2014. Relationship between wind speed and gas exchange over the ocean revisited. Limnol Oceanogr. Methods 12, 351–362. https://doi.org/10.1029/92JC00188.

Wanninkhof, R., 1992. Relationship between wind speed and gas exchange. J. Geophys. Res. 97, 7373–7382. https://doi.org/10.1029/92JC00188.

Ward, N.D., Bianchi, T.S., Medeiros, P.M., Seidel, M., Richey, J.E., Keil, R.G., Sawakuchi, H.O., 2017. Where carbon goes when water flows: carbon cycling across the Aquatic continuum. Front. Mar. Sci. 4 https://doi.org/10.3389/fmars.2017.00007.

Ward, N.D., Bianchi, T.S., Sawakuchi, H.O., Gagne-Maynard, W., Cunha, A.C., Brito, D. C., Neu, V., de Matos Valerio, A., da Silva, R., Krusche, A.V., Richey, J.E., Keil, R.G., 2016. The reactivity of plant-derived organic matter and the potential importance of priming effects along the lower Amazon River. J. Geophys. Res. Biogeosciences 1–18. https://doi.org/10.1002/2016JG003342.

Ward, N.D., Keil, R.G., Medeiros, P.M., Brito, D.C., Cunha, A.C., Dittmar, T., Yager, P.L., Krusche, A.V., Richey, J.E., 2013. Degradation of terrestrially derived macromolecules in the Amazon River. Nat. Geosci. 6, 530–533. https://doi.org/10.1038/ngeo1817.

Ward, N.D., Richey, J.E., Keil, R.G., 2012. Temporal variation in river nutrient and dissolved lignin phenol concentrations and the impact of storm events on nutrient loading to Hood Canal. Biogeochemistry 111, 629–645. https://doi.org/10.1007/s10533-012-9700-9. Washington, USA.

Weiss, R.F., 1974. Carbon dioxide in water and seawater: the solubility of a non-ideal gas. Mar. Chem. 2, 203–215. https://doi.org/10.1016/0304-4203(74)90015-2.

Weiss, R.F., Price, B.A., 1980. Nitrous oxide solubility in water and seawater. Mar. Chem. 8, 347–359.

Xie, S.P., Carton, J.A., 2004. Tropical atlantic variability: patterns, mechanisms, and impacts. Geophys. Monogr. https://doi.org/10.1029/147GM07.

Xue, Z., He, R., Fennel, K., Cai, W.J., Lohrenz, S., Huang, W.J., Tian, H., Ren, W., Zang, Z., 2016. Modeling pCO2 variability in the Gulf of Mexico. Biogeosciences 13, 4359–4377. https://doi.org/10.5194/bg-13-4359-2016.

Yeung, L.Y., Berelson, W.M., Young, E.D., Prokopenko, M.G., Rollins, N., Coles, V.J., Montoya, J.P., Carpenter, E.J., Steinberg, D.K., Foster, R.a., Capone, D.G., Yager, P. L., 2012. Impact of diatom-diazotroph associations on carbon export in the Amazon River plume. Geophys. Res. Lett. 39 https://doi.org/10.1029/2012GL053356. L18609.

Yin, X., Boutin, J., Martin, N., Spurgeon, P., Vergely, J.-L., Gaillard, F., 2014. Errors in SMOS Sea Surface Salinity and their dependency on a priori wind speed. Remote Sens. Environ. 146, 159–171. https://doi.org/10.1016/j.rse.2013.09.008.

Zhu, Y., Shang, S., Zhai, W., Dai, M., 2009. Satellite-derived surface water pCO2 and air-sea CO2 fluxes in the northern South China Sea in summer. Prog. Nat. Sci. 19, 775–779. https://doi.org/10.1016/j.pnsc.2008.09.004.